Image Cover Sheet

CLASSIFICATION	SYSTEM NUMBER 34912
UNCLASSIFIED	

TITLE

DETECTION AND IDENTIFICATION OF BURIED ORDNANCE BY MAGNETIC AND ELECTROMAGNETIC MEANS

System Number:

Patron Number:

Requester:

Notes:

DSIS Use only:

Deliver to: JR

UNCLASSIFIED

DEFENCE RESEARCH ESTABLISHMENT SUFFIELD
RALSTON ALBERTA

SUFFIELD REPORT NO. 283

DETECTION AND IDENTIFICATION OF BURIED ORDNANCE BY MAGNETIC AND ELECTROMAGNETIC MEANS (U)

by

Y. Das, J.E. McFee and M. Bell

Project No. 27B10

UNCLASSIFIED

TABLE OF CONTENTS

DEFENCE RESEARCH ESTABLISHMENT SUFFIELD
RALSTON ALBERTA

SUFFIELD REPORT NO. 283

DETECTION AND IDENTIFICATION OF BURIED ORDNANCE BY MAGNETIC AND ELECTROMAGNETIC MEANS (U)

by

Y. Das, J.E. McFee and M. Bell

ABSTRACT

There is presently a need for clearing old army ranges of buried unexploded munitions (UXM). The present operation which relies on conventional metal detectors is very slow and expensive - mainly due to the inability of these detectors to provide any information as to the depth, size or nature (shrapnel or UXM) of detected objects. This paper discusses the research effort of the Mines and Range Clearance Group at DRES, towards conceiving and implementing intelligent detectors, which could provide ordnance depth, size and possibly identity. In particular, the analysis of magnetic anomaly and pulse eddy current signatures of typical ordnance are discussed. Signal processing problems specific to these applications are indicated and the viability of various feature selection, extraction and recognition schemes are discussed.

(U)

DEFENCE RESEARCH ESTABLISHMENT SUFFIELD
RALSTON ALBERTA

SUFFIELD REPORT NO. 283

DETECTION AND IDENTIFICATION OF BURIED ORDNANCE BY MAGNETIC AND ELECTROMAGNETIC MEANS (U)

by

Y. Das, J.E. McFee and M. Bell

I. INTRODUCTION

This paper is primarily concerned with the analysis of magnetic anomaly and pulse eddy current signatures produced by buried unexploded munitions (UXM) and shrapnel. First, however, it is necessary to provide a brief background of the range clearance problem in order to provide perspective in viewing such analyses.

Some old Canadian military ranges, originally isolated, have now become attractive, potentially useful real estate resulting in periodic pressures on the government to release such lands for civilian use. At the same time trespassers in such areas and soldiers on active training ranges have been killed by the explosion of old munitions. It is thus necessary that such lands be cleared of UXM, although the philosophy of when and where to clear and alternatives to clearance is a complex one into which we shall not delve. At the same time, the present

operation of locating and clearing UXM is extremely labour intensive and expensive and needs improving.

The present objective of the range clearance program is to establish methodologies for the detection of UXM subject to a number of requirements. In brief these are:

Minimization of manpower requirements through
- determination of depth, position and size of object
- discrimination between UXM and false alarms
- design of rapid scan detectors.

Real time operation. This may be relaxed if discrimination is very effective.

Penetration of at least 2 meters. Since in the Canadian environment, frost can penetrate up to 2m, frost upheaval can bring to the surface any object buried at a lesser depth than this.

Over the last two years, a large number of possible methods for UXM detection have been investigated and it is possible to classify them under these broad headings:

Short Term Methods - those capable of development for prototype use in the next few years. There are two of these, namely:
- Magnetometer
- Electromagnetic Pulse Induction

These would appear to be the most promising techniques and will be the main subject of this paper.

Long Term Methods - those which will need technological development before they become feasible. Included in this classification are:
- Imaging - Electromagnetic and Acoustic
- Time Domain Reflectometry - Electromagnetic and Acoustic

Unlikely Methods - those which appear superficially feasible but under careful scrutiny are seen to be either unusable due to their fundamental physical principles or which will require major tech-

nological breakthroughs to be feasible. Several of these have the ability to detect the explosive itself, which would make them most desirable. There are many of these, a partial list being:

- METTRA (metal ReRadiation) - detection of metal contacts due to reradiated harmonics
- Nuclear Reactions - neutron capture spectroscopy, x-ray backscatter
- Trace Gas Analysis
- Biodetectors - olfaction, bioluminescence, biomagnetism
- Human Perception Channels.

On a typical range, one finds a mixture of shrapnel and UXM both of widely varying sizes in a mass ratio of between 10:1 and 100:1. The UXM is usually sparsely distributed and both it and shrapnel may lie at any depth between 0 and the maximum depth for the given munition. Further, although there is a statistical distribution of depths for a given munition, the maximum depth is reasonably well defined [1]. Thus, although a knowledge of object size will not discriminate between shrapnel and UXM, it may yield, together with depth information, an informed guess as to the object's identity. Depth and size information can help in other ways. Knowledge of depth can greatly speed UXM neutralization by eliminating unnecessary cautious digging whereas knowledge of size may determine the degree of care that must be exercised if an object is assumed to be UXM. Magnetometers and pulse eddy current detectors can determine location and depth and under certain conditions, size of a ferrous or conductive object, with good accuracy.

II. MAGNETIC ANOMALY ANALYSIS

A ferrous object may in general have associated with it a magnetic moment composed of a remnant and an induced magnetic moment. The former, often called a permanent moment, depends upon the metallurgical properties of the material and the thermal, mechanical and magnetic history of the object [2]. It is independent of the ambient field and may or may not, depending on the method of creation of the moment, be related

to the size of the object. This latter trait can obviously, in some cases, cause serious problems for size determination.

An induced moment is one induced by the ambient magnetic field, which is for our purposes the earth's field. The earth's field at our location is approximately 60000 nT (nanoTeslas) and dips 17° from the vertical. An induced moment is proportional to the ambient field and thus for ready determination of the properties of an induced moment based on its magnetic field, the ambient field must be constant in space and time during the traverse of the magnetic sensors. The spatial variation of the earth's field is shown in Fig. 1 and is clearly negligible to us since the traverse distances we are concerned with are of the order of a few meters. Local anomalies due to magnetite or similar deposits may cause some problems but again these are generally spread over distances much larger than a few meters. Some temporal variations [3] (Fig. 2) may create more problems. Diurnal variations may exhibit changes of 100 nT or more whereas typical measured fields from moments induced in UXM are up to several hundred nT. Fortunately these are very slowly varying, (a scan taking $\sim$ 10 sec) and can thus be baseline compensated. Micropulsations, too, are negligible over our time scale. Magnetic storms, however, may have variations of several hundred gamma over short time periods. They may be compensated by use of a base reference station or by use of multiple sensors, operating in differential mode since all of the temporal fluctuations, being produced far away, have very small spatial gradients.

We now turn to the discussion of the magnetic moment induced in a buried artillery round. Such rounds are generally doubly tapered cylinders or tear drop shaped, and exact solutions for the induced moment are unattainable. One approach is to model the object by finite element analysis but this requires extensive computation and does not yield an analytic solution. As a compromise, to study general trends, the shells were assumed to be prolate spheroids in a constant ambient field. A straight forward but tedious analysis (Appendix A) shows that the induced moment, specified by a magnitude per unit volume, m, one polar angle, β,

and one azimuthal angle, ϕ_m, (Fig. 3) are functions of parameters related to the size and material properties of the object, the polar angle, Θ_o, of the earth's field and parameters, θ_3, the polar angle, and ϕ_3, the azimuthal angle of the symmetry axis of the spheroid. These latter parameters relate the orientation of the spheroid to the direction of the earth's field (Fig. 4, 5, 6). A real shell, of course, will not yield curves identical to the previous curves, but since shells are reasonable geometric approximations to spheroids, the general trends should hold and hence such curves may be empirically obtained. Thus, it is possible, in theory at least, to determine size information about a shell if the orientation parameters can be extracted. Clearly, too, we can see that a significant remnant moment, unless it is size dependent and consistent in orientation relative to the major axis, will eliminate size information. The existance of such moments can be determined through experiments and will be discussed shortly. It should be pointed out that a similar analysis of shrapnel is not possible due to its irregular shape, nor is it useful due to its random orientation.

We have seen that a knowledge of the location, depth, size of the magnetic dipole and orientation of dipole are necessary to determine the size, orientation and permeability of the object. We shall now look at how such information can be extracted from the magnetic field of the dipole.

Any dipole, be it induced or remnant, has associated with it a magnetic field, $\vec{H}$, whose familiar components [4], written relative to a body fixed spherical coordinate system (r, θ, ϕ) are (Fig. 7)

$$\vec{H} = H_r\hat{r} + H_\theta\hat{\Theta} + H_\phi\hat{\phi} \qquad (1)$$

$$H_r = \frac{M}{2\pi r^3}\,\mathrm{Cos}\theta$$

$$H_\theta = \frac{M}{4\pi r^3}\,\mathrm{Sin}\theta$$

$$H_\phi = 0$$

where $\hat{r}$, $\hat{\theta}$, $\hat{\phi}$, are the unit vectors and $M = |\vec{M}|$.

Since the orientation of the moment is not known in advance, it is necessary to obtain components relative to a known coordinate system which has been chosen in this instance to be a cartesian system with the z-axis being the vertical and the dipole lying in the xz plane. The sets of components are related through a cumbersome 3 x 3 rotation matrix which can be calculated and yields the following space fixed components (Appendix B).

$$H_z = \frac{M}{(x^2 + y^2 + z^2)^{5/2}}\left[\text{Cos } \beta(2z^2 - x^2 - y^2) - 3 \text{ Sin } \beta(xz)\right](4\pi)^{-1}$$

$$H_y = \frac{y}{z} H_z + \frac{M}{(x^2 + y^2 + z^2)^2} \frac{y}{z}\left[\frac{y^2z^2 + (xz \text{ Cos } \beta + z^2 \text{ Sin } \beta)^2}{(x + z \text{ Tan } \beta)^2 + y^2}\right.$$

$$\left. + \frac{(xz \text{ Sin } \beta + (x^2 + y^2) \text{ Cos } \beta)^2}{(x + z \text{ Tan } \beta)^2 + y^2}\right]^{1/2} (4\pi)^{-1} \qquad (2)$$

$$H_x = \frac{x}{z} H_z + \frac{M}{(x^2 + y^2 + z^2)^2} \frac{(x + z \text{ Tan } \beta)}{z}\left[\frac{y^2z^2 + (xz \text{ Cos } \beta + z^2 \text{ Sin } \beta)^2}{(x + z \text{ Tan } \beta)^2 + y^2}\right.$$

$$\left. + \frac{(xz \text{ Sin } \beta + (x^2 + y^2) \text{ Cos } \beta)^2}{(x + z \text{ Tan } \beta)^2 + y^2}\right]^{1/2} (4\pi)^{-1}$$

In general, however, we must also include the ambient magnetic field intensity, $\vec{H}_o$, such as that of the earth. Thus:

$$\begin{aligned} H_{Tx} &= H_x + H_{ox} \\ H_{Ty} &= H_y + H_{oy} \qquad (3) \\ H_{Tz} &= H_z + H_{oz} \\ \vec{H}_T &= \vec{H} + \vec{H}_o \end{aligned}$$

where $\vec{H}_T$ is the total magnetic field intensity with cartesian components H_{Tx}, H_{Ty}, H_{Tz}. The magnitude of the components of the dipole field tend to be at least 2 orders of magnitude less than that of the ambient field.

Since the orientation of the dipole is unknown, one can measure only H_{Tz}, a linear combination of H_{Tx} and H_{Ty} (with unknown mixing ratio) or the total field which to second order is given by (Appendix B):

$$H_T - H_o \approx H_x \text{ Sin } \theta_o \text{ Cos } \phi_o + H_y \text{ Sin } \theta_o \text{ Sin } \phi_o + H_z \text{ Cos } \theta_o \quad (4)$$

$$+ \frac{1}{2H_o}\left[H^2 - (H_x \text{ Sin } \theta_o \text{ Cos } \phi_o + H_y \text{ Sin } \theta_o \text{ Sin } \phi_o + H_z \text{ Cos } \theta_o)^2\right]$$

where $H_T = |\vec{H}_T|$ $H_o = |\vec{H}_o|$ $H = |\vec{H}|$ and

θ_o, ϕ_o are the polar and aximuthal angles respectively of the ambient field with respect to the cartesian system.

There are two basic types of magnetometer sensors, namely total field, e.g. cesium vapour, proton precession [5], and vector, e.g. fluxgate, super conducting Josephson junctions [6], [7]. The former measure only the magnitude of the total magnetic field (and not its direction) which is to first order (terms not in brackets in (4)) the projection of the dipole field along the ambient field direction. The latter type of sensor measures the field in a particular direction determined by the sensor orientation and thus requires a choice of axis. Vector magnetometers are very sensitive to misalignment relative to one another. This is in essence due to the large value of the ambient (earth's) field with respect to the dipole field (often 100:1) and manifests itself as large low frequency baseline shifts. This can be corrected by building precisely aligned rigid arrays and such a 3 sensor fluxgate array has been designed and constructed by this laboratory. This alignment problem is not found for total field sensors. Since all components are, on the average, the same in magnitude, the only criterion for choice of axis is mathematical simplicity to enhance computational speed. Clearly, then, the z-component is the best choice.

Finally, we note that any one of the components of the field at a point on a two dimensional grid is a function of the coordinates, x, y, z, the angle of the dipole axis relative to the vertical, β, and

the magnitude of the magnetic moment, M. This is illustrated in Figs. 8, 9, 10 by two dimensional maps of lines of constant field intensity (vertical component) for dipoles with parameters typical of buried ordnance. For the vertical component, the contour maps are symmetrical about the x-axis and range from radially symmetric for $\beta = 0°$ to antisymmetric about the y-axis for $\beta = 90°$. The contours for given β remain a similar shape but shrink in dimension as z decreases and their intensity is directly proportional to M. Contours for x and y components may have similar shapes as well as biaxially symmetric forms.

It should be noted that in the above analysis, it was assumed that the object could be represented as a magnetic dipole. Higher order multipoles manifest themselves as additional terms to the polar components of the field and considerably complicate the cartesian components. Fortunately, they fall off with distance from the object much faster than does the dipole field and, as we shall see from our experiments, are negligible over the range of distances of interest. Even irregularly shaped shrapnel appear to be dipoles at these distances.

We shall now deal exclusively with sensors moving roughly in a plane perpendicular to the z direction. Deviations from a plane can be compensated for by a method to be described and this will be discussed later. We assume that one or more magnetic sensors sweeps in a straight line in the x-y plane. Thus by choosing the sweep direction as the y'-axis, a new right handed coordinate system x'-y'-z' may be chosen with arbitrary but known x'-y'-origin and the dipole located at coordinates (x_o', y_o', o) in the primed system and (o, o, o) is the unprimed system. The angle of the x'-axis relative to the x-axis is given by α (Fig. 11) and thus the coordinates are related by a rotation matrix in the following manner:

$$\begin{bmatrix} x \\ y \\ z \end{bmatrix} = \begin{bmatrix} \cos\alpha & \sin\alpha & 0 \\ -\sin\alpha & \cos\alpha & 0 \\ 0 & 0 & 1 \end{bmatrix} \begin{bmatrix} x' - x_o' \\ y' - y_o' \\ z' \end{bmatrix} \qquad (5)$$

Knowing x_o', y_o' and α eliminates any problem surrounding the specific

choice of x-axis and origin mentioned earlier and thus everything is known about the dipole if the six parameters - x_o', y_o', z, α, β, M, are known. It would initially appear (4) that for total field measurements more parameters would be required. This, however, is not the case, since θ_o is a known or measurable constant for a given geographical location and the sensor traverse bearing angle, ϕ_B, is easily monitored to determine ϕ_o:

$$\phi_o = \phi_B - \alpha - \pi/2 \qquad (6)$$

A number of clever attempts have been aimed at determining these parameters through a knowledge of the distribution of one or more components of the dipole field, superimposed on the earth's ambient magnetic field, which is as previously mentioned 10^2 to 10^5 times larger. Space does not permit a discussion of all methods available, but some of the more common techniques include graphical interpretation [8], [9], profile matching techniques either in configuration space [8] or reciprocal space, specialized geometry methods [10], [11], [12] and the powerful method of inversion of the field derivative equations [13]. These previous attempts, however, have generally all incorporated a number of restrictions which have been acceptable for the situation in question but which would not permit more general usage. In some cases [13] only a few data points have been used requiring a high signal-to-noise ratio. In others [3], the magnetic field sensor (magnetometer) has been required to pass directly over the object. Assumptions are often made concerning the orientation of the dipole relative to the earth's field [11], [14], the vertical [10] or the object's orientation [3]. The assumption is commonly made that the sensor is stationary or is in a fixed horizontal plane [2], [3]. Also it is frequently assumed that the total field is the sum of the ambient field magnitude plus the component of the dipole field projected onto the ambient field's direction [3]. Some techniques have been designed for single sensor use [10] or require a knowledge of the field gradient [13] and some are not real time techniques, such as those which match characteristic profiles after the fact [8], [9].

Two methods have been developed by the authors which appear to be of use in extracting dipole parameters from measured field data. The methods have been developed, keeping in mind several points:

(i) Assumptions have been minimized.

(ii) Real time operation is highly desirable.

(iii) It is desirable not to halt the search vehicle.

(iv) Methods involving the true gradient cannot be used since they assume sensor spacing is small with respect to distance from the dipole. This cannot be achieved for our small sensor-to-dipole spacings due to finite sensor size and sensor cross talk.

(v) The special properties of the vertical component of the dipole field should be exploited, namely
- symmetry about the x axis (Figs. 8, 9, 10)
- extrema located on the x axis (Figs. 8, 9, 10)
- low spatial frequencies (Fig. 11).

We shall now discuss the two methods in more detail.

A. Profile Match Method

Probably the simplest technique in concept and one which, unlike many other methods, can be model independent, is that of comparing a sampled field distribution with a series of stored profiles. Preserving the salient features of the field profiles in real space would generally require prohibitively large amounts of computer memory but one can make use of the low spatial frequency properties of the profiles by storing Fast Fourier Transforms (FFT's) of representative profiles for comparison, by criteria such as least squares, with measured FFT's. This procedure has been computer simulated using profiles both with and without typical gaussian noise of up to 4 nT. Using up to three parallel sensor profiles spaced 25 cm apart and an origin coinciding with the point of closest approach, it was possible to identify dipole parameters to within 6.25 cm in depth,

12.5 cm in distance of closest approach, 11.25 degrees in horizontal and vertical angles and a few percent in moment value using 5500, 40 element stored FFT's. The range of parameters was 12.5 to 250 cm for z, 0 to $\pi/2$ for β, 0 to 2π for α, 0 to 250 cm for the distance of closest approach. Since M is a simple scale factor for the magnetic field values it was determined by normalizing to the largest spectral value, classifying by least squares and then multiplying the normalization factor for the best fit times the moment value of the reference FFT. Although real time was not achieved using the IBM 1130 computer it was calculated that this may be achievable using a dedicated fast minicomputer particularly if the range of β can be reduced to less than theoretical maximum range of 0 to π (Fig. 5). Erroneous parameter sets could be selected when single sensor profiles with or without noise were used, a fact that can be theoretically shown. This can be and was eliminated by use of multiple parallel path sensors. It should be noted that in field operations, measured and best estimate stored profiles must have a common origin, otherwise the spectra will differ by an indeterminate frequency dependent phase shift which prohibits least squares comparison. In theory, if one samples the profiles for some preset interval on either side of an extremum, this problem could be eliminated, although experiments have yet to be carried out utilizing this idea.

B. Model Fitting Method

Assuming that the field of the anomaly can be adequately represented by that of a dipole, one can model the sampled magnetic data by the equations (2) to (5). As stated before, there will in general be 6 parameters which can be floated and some iterative technique must be employed to vary the parameters until the fitted function agrees with the sampled data to within a specified accuracy. Such a method has previously been employed for submarine detection using a Newton Raphson iterative scheme [12], but simplifying assumptions were made to reduce the number of free parameters, presumably because the multiparameter Newton Raphson technique is quite slow. A much faster method would be nonlinear least squares

fitting, provided a method could be found for which convergence was independent of initial estimates of parameters.

Marquardt's nonlinear least squares algorithm [15] has the capability to converge to a global minimum in χ^2 space independent of initial choice of parameters, provided the χ^2 surface is smooth and has no local minima. Other algorithms, such as Fletcher-Powell minimization [16], are faster than Marquardt's but are valid only near a minimum in the space and hence do not have the required insensitivity to initial parameter guesses. The algorithm, which was originally designed for one dimensional data, has been adapted by the authors to process the two dimensional arrays of magnetic data.

The following is a description of the two dimensional generalization of Marquardt's nonlinear least squares fitting algorithm which has been adapted from the one dimensional code of Bevington [17]. Additional modifications have been made to enhance speed but these will not be discussed further.

We define a model function $f(x,y,\vec{a})$ and a two dimensional sampled array of data $g(x_i,y_i)$ which together form a χ^2 space with minimum $\chi_o{}^2$. We can define a matrix $\overline{\overline{\alpha}}$ by

$$\alpha_{jk} = \sum\sum x_i y_i \left(\frac{\partial f}{\partial a_j}\right|_i \left(\frac{\partial f}{\partial a_k}\right|_i W_i \qquad (7)$$

$$\equiv \frac{1}{2}\left(\frac{\partial^2 \chi}{\partial a_j \partial a_k}\right| \quad \chi^2 = \chi_o{}^2$$

where α_{jk} is an element of $\overline{\overline{\alpha}}$

a_k is an element of $\vec{a}$, the parameter vector

subscript "i" denotes evaluation of variable at sampled coordinates x_i,y_i

W_i are the weights at each point x_i,y_i

We also define a vector $\vec{\beta}$ by

$$\beta_k = \sum\sum x_i y_i \quad (g_i - f_i) \left(\frac{\partial f}{\partial a_k} \right|_i \tag{8}$$

$$\equiv -\frac{1}{2} \left(\frac{\partial \chi^2}{\partial \alpha_k} \right| \quad \chi^2 = \chi_o{}^2$$

and a new matrix $\overline{\overline{\alpha}}'$ by

$$\alpha_{jk}' = \alpha_{jk}(1 + \lambda) \qquad \text{for } j = k \tag{9}$$

$$= \alpha_{jk} \qquad \text{for } j \neq k$$

Close to a minimum in χ^2-space it may be shown [17] by expansion of the model function that

$$\beta_k = \sum_j \delta a_j \alpha_{jk} \tag{10}$$

where δa_j is an arbitrary, small increment in the Taylor expansion about the minimum of χ^2 as a function of $\vec{a}$

Thus, we define

$$\beta_k' = \sum_j \delta a_j \alpha_{jk}' \tag{11}$$

Far from a minimum, we choose λ large with respect to 1 such that

$$\beta_j' \approx \lambda \alpha_{jj} \delta a_j \tag{12}$$

Thus, the parameter increments are in the same direction as the gradient and are scaled by the factor $(\lambda \alpha_{jj})$. This is equivalent to a gradient search method.

Close to a minimum, λ is chosen small with respect to 1 and thus β_k has the same form as (10). This is clearly equivalent to linearization of the model function. It can be seen that by appropriate choice of λ the gradient search technique can be employed far from a minimum where the linearization method is not valid (and might yield erroneous curvatures) and one can switch to the linerarization method when it becomes valid.

The algorithm to automatically scale λ is given in [17]. It essentially consists of comparing the old and new chisquares from successive iterations and increasing λ if the new χ^2 exceeds the old.

The general geometry for obtaining the magnetic data is shown in Fig. 12. There are two approaches, the stationary method and the dynamic method. Both may employ vector or total field sensors measuring the difference in field between them (gradiometer or difference mode) or the individual field at each (magnetometer mode). The array does not necessarily have to be horizontal for the algorithm to function properly and may be man- or vehicle-portable.

In the stationary approach, the array of sensors scans the terrain until a significant field value, possibly a maximum is encountered by the sensors and there a stationary measurement is taken. An array of at least six sensors, in general, or five if a maximum is detected, must be employed to solve a system of six nonlinear field equations by least squares means as described above. The chief advantages of this method are adaptability for man portable use and the lack of knowledge required concerning sensor motion. The chief disadvantages besides requiring stoppage of sensors, is a lack of immunity to noise. For situations encountered in UXM detection where maximum signal-to-noise ratios of 50 or less are common the minimal number of sensors can yield ill-conditioned sets of equations and hence a variety of different, nonunique solutions. Time averaging can minimize this at the expense of increased measuring times. Multiple solutions because of the low number of data points compared to number of parameters, can be minimized by increasing the number of sensors. This, however, may make the system overly cumbersome for man-portable use.

The dynamic method lessens problems associated with ill-conditioning by acquiring information from multiple measurements. Essentially, the method consists of sampling the dipole field at fixed intervals by sensors whose position relative to each other and a common origin is known. Sampled data is stored in a buffer to determine the ambient magnetic field baseline for subtraction and as new data is input, the oldest data is overwritten. This continues until field values significantly in excess of

baseline fluctuations occur at which time sampling is allowed to continue for an additional preset time. After this time interval which is slightly greater than the duration of the longest profiles expected, the sampling halts and the data is subjected to the six parameter two dimensional weighted nonlinear least squares fitting procedure.

If the number of data points is small (which we shall see is generally true), it is feasible to use multiple commutating buffers so that the data can continue to be acquired during analysis, rather than halting the sampling. As in the case of profile matching, the field component equations show that there are a number of cases where two significantly different parameter sets can yield the same sampled field profile for a given component. The use of more than one sensor eliminates this problem. The dynamic method, of course, requires a knowledge of the sensor positions where the field measurements are made. One way of doing this is to attach an inertial guidance package to the array.

In order to determine speed of the algorithm and the ability to converge to the correct parameter set (as determined by the shape of the χ^2 space), a computer code was written incorporating the algorithm to simulate a horizontal linear array of up to 10 magnetic sensors (either vector or total field) operating in magnetometer mode or difference mode relative to the center sensor, moving with known, not necessarily constant, velocity near a buried dipole in the manner previously described and attempting to extract the dipole parameters. It was noted that sensor spacing, $\Delta x'$, and sampling distance, $\Delta y'$, number of sensors, n_x, and number of sample points per sensor, n_y, affect computational speed and shape of the χ^2 space. Optimum values for these quantities could be obtained from the simulation. The code was written to include electronic and sensor noise as well as measurable deviations of the sensors in the x', y', and z' coordinates due to roll, pitch and yaw of the array and variations in velocity. Dipole parameters were randomly chosen from the range of possible values for each and the initial guesses were taken as the midpoints of the ranges for each. Parameter ranges were chosen from those applicable to buried

artillery shells, namely $.25 \leq z \leq 2.00m$, $0 \leq \beta \leq \pi$, $-.5 \leq x_o' \leq .5m$, $-.5 \leq y_o' \leq .5m$, $0 \leq \alpha \leq 2\pi$, $.06 \leq M \leq 6.0A\ m^2$, although the code is applicable to other situations.

In preliminary tests, two problems were encountered, namely convergence to a local minimum with reduced $\chi^2 > 10$ and attempted convergence to a local minimum with very large χ^2 and at least one very large parameter. Although these situations were circumvented by appropriate tests in the code, approach of such conditions degraded computational speed and thus it was felt best to minimize the occurance of such situations. Simulations were performed on over 100 different random parameter sets for vertical axis sensor arrays in magnetometer and gradiometer modes and total field sensor arrays. Occurance of the above mentioned problems was minimized by choice of geometry constants; $n_x = 3$, $\Delta x' = .25m$, $n_y = 20$, $\Delta y' = .5m$ for the first two array types and $n_y = 40$, $\Delta y' = .25m$ for the last type. A sensor noise band of 1 nT was used as being representative of achievable values for moving fluxgate and cesium vapour sensors. In all cases, the program converged to yield the correct parameter set with reduced χ^2 between 0.6 and 1.2, and no local minima with reduced $\chi^2 < 10$ or additional extrema were encountered. In all cases the dipole parameters were correctly determined to within a few percent and often to within less than one percent. Run times for 85% of all cases on an IBM370/158 were less than 12 s (vertical-axis sensors in magnetometer mode), 12 s (vertical-axis sensors in gradiometer mode) and 73 s (total field magnetometer). Time per iteration was constant at .48 s, .54 s and 1.98 s respectively.

The computation times mentioned are equivalent to pseudo-real-time operation, and fast minicomputers are available which can increase the speed of this algorithm by 25%. For buried ordnance, assuming a maximum vehicular speed of 4 km/hr, these times correspond to a "dead zone" of 10 m for the first two array types and 60 m for the third type. This is quite reasonable, since ordnance spaced closer together is usually accompanied by prohibitive amounts of extraneous background clutter, in the form of

shrapnel. Of course, as already mentioned, these zones can be decreased almost to zero by the use of multiple buffers on input.

Finally, it is encouraging that parameters for dipoles whose flux density extrema did not exceed 15 nT (S/N = 15:1) were well approximated as well as were parameters yielding peaks of the order of 1000 nT (S/N = 1000:1).

One modification of the dynamic method may speed analysis by reducing the number of parameters. It is designed for use with only z-component measurements of the field. Since the extrema of the z component lie on the x axis of the anomaly, an extremum search could be employed to locate this axis. Sampled data points would be interpolated to yield field values on this axis. A five parameter nonlinear fit to the interpolated profile would then be done, again using the previous least squares fit routine although only a one dimensional algorithm would be necessary. Thus, with α known, it is possible to fit the axis profile. Studies must be undertaken to see if the time taken in extrema location and data interpolation is compensated by the time gained in reduction of the parameter space.

It should be pointed out, that in some of the above methods, detection is achieved after the sensor(s) have passed the object and thus some reference system must be used to keep track of the vehicle position to allow post-indication of the object.

A few assumptions have been made in the previous analysis. The dipole assumption is in general valid only at distances large with respect to a characteristic length (such as the mean chord length) of the object and at smaller distances higher order multipoles might become noticable. Correlated or non-gaussian noise have been neglected since, strictly speaking, least squares minimization maximizes the likelihood function only for gaussian statistics. The ratio of remnant dipole moment to induced moment is also not known. It was felt, then, that magnetic profiles of real ordnance should be obtained to verify validity of the analyses.

To this end, the test facility shown in Fig. 14 was constructed.

A shell or piece of shrapnel was passed on a "railway cart" running east-west under a stationary magnetometer array which was positioned at the mid-point of the track. Shell position was determined by position switches which alternately switched a flip-flop. Position accuracy was taken as ± 1 cm. The electronics box contained drive and sense circuitry for the fluxgate sensors plus battery power. A triangular drive waveform of approximately 31.4 KHz was employed in conjunction with a peak detection circuit designed in this lab. Sensor feedback [6] was not employed. The array chosen for the first set of tests was a vertical array consisting of three 2.5 cm diameter 4-79 permalloy ring core fluxgate sensors. Fluxgates were chosen due to their low cost, portability and directionality. Their noise properties, typically 0.5 nT for a 0 to 10Hz passband, were adequate for our purposes. Sense and drive windings were the same configuration as that of a Brown magnetometer [6]. The sensitive axes of the ring cores were aligned roughly vertically and then adjustment of amplifier gain was employed to equalize sensitivities. Vector magnetometer sensors, such as fluxgates, have a serious limitation in that they are severely orientation sensitive. This is primarily due to the order of magnitude difference between the ambient and dipole fields. The limitation can be defeated by using the magnetometer in a stationary manner, which is of course not practical for range clearance, or by aligning the sensors very accurately (< .01°) and operating in gradiometer mode. The former was done for the experiments that have been previously described since sensor motion was not required. This laboratory has recently completed construction of a three sensor fluxgate (vector) magnetometer theoretically capable of up to .0003° accuracy in alignment between sensors. This should allow measurement of gradients in the vertical field component accurate enough for our purposes for up to 10° roll and pitch of the sensor array.

Amplified sensor outputs and the position flip-flop output were fed to an oscilloscope for direct viewing and also to an ADC. Profiles were sampled, digitized and stored under control of a ProLog microprocessor system and were output on teletype or papertape to allow input to an IBM

1130 computer. The entire track, cart and frame assembly was made of wood.

Frequency histograms of the noise on two of the sensors are shown in Fig. 15. One can clearly see the strong gaussian shaped electronic/sensor noise component of approximately 1 nT and the weaker cusp shaped component which is presumably sinusoidal and may be related to low frequency staff oscillations. A baseline shift is also obvious in the middle sensor. The bandwidth employed was 0 to 10 Hz.

As a preliminary experiment, profiles were obtained for shell orientations of 0, 45, 90° with respect to the vertical and 0, 45, 90° with respect to the track direction, with the shell directly under the track. The dipole origin was assumed to be the center of mass and the symmetry axis was taken to be the equivalent spheroid 3-axis designated by polar angle θ_3 and azimuthal angle ϕ_3 as in Appendix A. Thirty-three profiles corresponding to depths of 70, 95 and 145 cm (± 1 cm) were obtained for a 105 mm shell and 60 and 70 cm for representative shrapnel. Each profile consisted of 256 samples obtained by pushing the shell over the 7 m length of the track at roughly uniform walking speed. A given profile took approximately 10 seconds to obtain which translates to a sampling rate of approximately 30 Hz or 70 cm/sec. Since the sensor passband cut off at 10 Hz, the Nyquist criterion was satisfied.

A code was written for the IBM 1130 computer to convert the papertape data to card format. This data was in turn used as input for an analysis code written to run on an IBM 370/158. The program first found the relative shell-sensor position for each sampled point by linearly interpolating the position sensing ("flip-flop") track. The profile was then fitted using as a model the vertical component equation plus a d.c. shift (7 parameters). The fitting routine used was the generalized Marquardt algorithm previously described. Reduced χ^2 values for the fitted function together with depth estimates and uncertainties are given in Table 1. Typical sampled profiles and fitted functions are shown in Figs. 16-19. The results were quite encouraging.

For an assumed R.M.S. sensor noise of 3 nT (chosen to include correlated noise), all profiles with maxima less than ~ 750 nT could be

fitted yielding reduced chi-squares of one or less. For those with values greater than 750 nT, sensor nonlinearities affected the fit, making chi-squares from 4 to 25 times higher.

Correlated noise did not cause any apparent deterioration in goodness of fit, although it did appear to cause an overestimation of the variance of the noise band.

Estimates of depth (Table 1) were good for most profiles, even for poorer fits, deviating on average by no more than 5 cm from the correct values. This error may be explained in part by the fact that the dipole origin and shell center of mass do not necessarily coincide. The explanation is reinforced by the observation that most depths are consistently slightly low.

Extracted magnetic moment data are shown in Figs. 20-22 for a 105 mm shell and an essentially intact but hollowed out piece of 105 mm shrapnel. Since the effective volume of the shells was not known, the values of m were normalized to the maximum value for each object. It is interesting to note that although the "m" curves are in rough agreement between shell and shrapnel, the β and ϕ_m curves are substantially different. In addition, it is found that the curves disagree sharply with curves derived from the spheroidal model using parameters typical of a 105 mm shell (Appendix A). This could be caused by 1) large ambient field gradients, 2) shift of the ambient field direction, 3) the presence of permanent magnetic moments in the objects or 4) lack of validity of the spheroidal model. The first and second possibilities would presumably be due to ferrous materials in the room. The first possibility was discounted because good fits to a single dipole were obtained and very large gradients are required to substantially alter the induced moments (Appendix A). Using orientations of ambient field differing from that of the earth for the model curves did not improve the agreement, thereby eliminating the second explanation. Thus, the possibility exists of permanent magnetic moments being present, which if true, would hamper size determination. Finally it is interesting that, although single profiles were

fitted, no examples of multiple solutions for a given profile arose. This is presumably attributal to the fact that although such cases can theoretically exist, they are not common for high signal-to-noise ratios.

A number of areas still remain to be investigated. The effect of magnetic background due to random dipoles, such as shrapnel, must be studied. If this proves to be troublesome, surface clearance (pickup of all surface lying ferrous objects) may be employed. Magnetite bearing soil may also contribute a troublesome background signal. The ability to distinguish and extract parameters from UXM lying close together must be ascertained. As the previous experiments have shown, the dipole approximation is valid for minimum shell-to-sensor distances of 60 cm. For smaller distances such as might be encountered for small UXM lying very close to the surface, the effect of higher order multipoles must be explored. Finally, methods of cheaply monitoring the motion and position of the sensor array should be investigated.

Testing of the precise alignment fluxgate array, previously mentioned, will commence soon. Feedback systems, to improve linearity of fluxgate sensors, are being investigated. Ring cores of 6-81 permalloy with improved noise characteristics and temperature sensitivity have been obtained and will be tested. Finally, a nonmetallic building has been constructed complete with a set of large Helmholtz coils. This will allow experiments in small gradient ambient field conditions in order to carry out the previously mentioned investigations.

III. ANALYSIS OF PULSE EDDY CURRENT SIGNATURES

The purpose of this section is to give a brief overview of the research aimed towards the development of a metal detector, based on the pulse induction principle, which may provide information as to the depth, size and type of a buried artillery round. Basically, the method relies on the fact that when a conducting object (permeable or non-permeable) is subjected to a steptype magnetostatic field, eddy currents are generated in it, which subsequently decay in a manner characteristic of the object's size and its material properties. An analysis of the voltage induced by

these eddy currents should, in principle at least, provide information about the object.

1. Geometry and Signal: A pulsed magnetic field is produced by driving a current pulse through a coil of wires (Fig. 23). Subsequent to the collapse of the drive pulse, the decaying eddy currents in the object induce a voltage in a receive coil. The question of sensitivity and the design of suitable coils and electronics for such a system will not be discussed here.

Since the shapes involved do not permit a ready electromagnetic analysis, as a first step, they have been modelled by 'equivalent' spheres which have the same surface areas as the rounds. For lack of a better method, at this moment, any effect of shape and orientation has to be determined from measurements.

The signal induced by a sphere of radius, a, conductivity, σ, and relative permeability, μ_r, is given by [18] ($t > 0$):

$$V(t) = \frac{CR_{1,2}^2}{(R_T^2+d_T^2)^{3/2}(R_{1,2}^2+d^{2})^{3/2}} \cdot \frac{a}{\sigma} \sum_{n=1}^{\infty} A_{k_n} \; e^{\frac{-k_n^2 t}{\mu\sigma a^2}} \qquad (13)$$

The constant C is given by

$$C = \frac{\pi N_T N_{1,2} R_T^2 I_T}{2}$$

where

N_T = number of turns of the transmit coil

$N_{1,2}$ = number of turns on receive coils 1 or 2

I_T = peak current in the transmit coil.

Other symbols in (13) are defined as follows:

d_T = distance to object centre from transmit coil centre

$d_{1,2}$ = distance to object centre from centres of receive coils 1 or 2 respectively

$R_{1,2}$ = radii of receive coils 1 or 2 respectively

R_T = radius of transmit coil

t = time measured from the instance of collapse of the transmit current

$\mu = \mu_o \mu_r$

$\mu_o = 4\pi \times 10^{-7}$ H/m

$$A_{k_n} = 6k_n^2/((\mu_r-1)(\mu_r+2) + k_n^2) \qquad (14)$$

and k_n's are the solutions of the trancendental equation

$$\tan k_n = \frac{k_n(\mu_r-1)}{k_n^2 + (\mu_r-1)} \qquad (15)$$

The properties of the solution to (15) and of the signal represented by (13) will be discussed later, but first we shall discuss how depth can be determined by using (13).

2. Determination of Depth: The concept of using signals induced in two receive coils to determine the depth of a detected object has been applied before. We, however, have carried out extensive investigation of the suitability of various coil sizes and configurations. In the following, an outline of the principle and some typical calibration curves will be presented. One of the configurations studied consists of two receive coils of radii R_1 and R_2 separated vertically by an amount $d_1-d_2 = \Delta d$ (Fig. 23). The ratio of signals in R_1 and R_2 at time t_i is given by (assuming $N_1 = N_2$)

$$VR(t_i) \equiv \frac{V_{R_2}(t_i)}{V_{R_1}(t_i)} = \frac{R_2^2(R_1^2+(d_2-\Delta d)^2)^{3/2}}{R_1^2(R_2^2+d_2^2)^{3/2}} \qquad (16)$$

Knowing $VR(t_i)$, R_1, R_2 and Δd, the distance d_2 from R_2 can be determined. In practice the average value of $VR(t_i)$ over a number of t_i's should be

used. Normalized depths (d_2/R_2) are plotted against voltage ratios for various R_1/R_2 in Fig. 24 for a given separation of coils. The parameters should be chosen to obviate multiple positive real solutions for d_2. It is apparent from these curves that depth could be reliably determined using these configurations only over a certain range. A final choice of coil configuration has not yet been made.

3. Properties of the Signal: We will now briefly describe the properties unique to the signal at hand in order to point out the difficulties involved in extracting information about the object from such a signal.

The salient features can be described by looking at the time-varying part of Equation (13) which is:

$$u(t) = \sum_{n=1}^{\infty} A_{k_n} e^{-\alpha_{k_n} t} \qquad (17)$$

This is a series of damped exponentials with decay constants given by

$$\alpha_{k_n} = k_n^2/(\mu_o \mu_r \sigma a^2), \quad n = 1, 2, 3 \ldots\ldots\ldots \qquad (18)$$

where $\alpha_{k_1} < \alpha_{k_2} < \alpha_{k_3} < \ldots\ldots\ldots < \alpha_{k_{n-1}} < \alpha_{k_n}$

The variation of k_n with μ_r and n is shown in Table 2. For non-permeable objects (μ_r=1), the k_n's are simple multiples of π, namely $n\pi$, while for permeable objects they are slightly higher than $n\pi$, depending on μ_r, and reach a limiting value as μ_r increases. The values of k_n are such that the values of the decay constant α_{k_n} increase more rapidly with n for a non-permeable than for a permeable object.

The most interesting feature and also a source of difficulty in extracting object parameters is how the amplitudes A_{k_n}'s are related.

$$A_{k_1} = A_{k_2} = \ldots\ldots\ldots\ldots = A_{k_n}, \quad \mu_r = 1 \qquad (19)$$

For a permeable body, A_{k_n} starts off with a small value for n = 1 and increases slowly with n, reaching, in the limit, the value for the non-permeable case.

Figs. 25 and 26 show the behaviour of the first ten terms respectively for a non-permeable and a permeable body. In the non-permeable case, the higher order terms decay significantly after a "sufficient" time interval and the first order term dominates the response. But in the permeable case, since the terms which decay faster have higher initial amplitudes, no section of the response with amplitude sufficient for analysis can be identified as being dominated by any particular term. This precludes the use of a well-known method used in related fields, where the tail of the response is analysed to estimate the dominant decay factor for a non-permeable object. Further, in our particular application, the signal strengths involved (due to the distances between the coils and the object) are usually low and the tail of the response, in such cases, might have too low a signal-to-noise ratio to allow such an estimate even for a non-permeable object.

4. Signal Analysis: The question of real time operation will be set aside for the moment. Given a set of measured samples of a signal of the form

$$u_i \equiv u(t_i) = \sum_{j=1}^{N} A_j e^{-\alpha_j t_i} + \text{Noise}, \quad i = 0, 1, 2, \ldots\ldots M-1 \quad (20)$$

information about the parameters of the sphere, namely μ_r, σ, and a could be obtained if we could extract the A_j's and the α_j's reliably. Two methods address this problem - one is a nonlinear least-square fitting [17] and the other is Prony's algorithm [19]. These two methods were investigated to establish their suitability in analysing typical signals for our application.

A. Nonlinear Fitting: Theoretically, nonlinear fitting of the data, u_i, with a function of the type, $y(t) = \sum_{j=1}^{NT} \overline{A}_j e^{-\overline{\alpha}_j t}$, could

provide estimates $\bar{A}_j$, $\bar{\alpha}_j$ of the required parameters A_j and α_j respectively. However, nonlinear fitting is difficult at best and its success is very much dependent on the fitting function itself. It is very time-consuming for any reasonable number of unknown parameters and often requires a "good" initial guess of the parameters to be estimated. Further, to make matters worse, in our application the functions involved are highly damped real exponentials which are strongly correlated with each other - making accurate estimates of parameters α_j, very difficult. The need to use a high value of N (for permeable objects) adds further to this difficulty. Thus in our particular application, it is doubtful if this method would be useful in the field. However, this method was investigated as a potential tool for analysing data measured in the laboratory to establish the effect of shape and orientation of the decay factors and amplitude coefficients. This would be facilitated by the fact that laboratory data can be obtained with high signal-to-noise ratios, and analysed on a general purpose computer with no real time restriction. Also, in the laboratory situation, the magnitude of the problem could be drastically reduced by knowing the permeability of the object under test, since if μ_r could be assumed known, then all the A_j's and α_j's could be related to only one fundamental amplitude and decay constant respectively - thus reducing the number of unknown parameters to be estimated to only two.

In particular when μ_r=1, the fitting function could be be reduced to

$$y(t) = \sum_{j=1}^{NT} \bar{A}_1 e^{-j^2 \bar{\alpha}_1 t} \qquad (21)$$

and only $\bar{A}_1$ and $\bar{\alpha}_1$ would have to be determined. For $\mu_r \neq 1$, the relation between the $\bar{A}_j$'s and $\bar{A}_1$, and between the $\bar{\alpha}_j$'s and $\bar{\alpha}_1$, would be known from a solution of Equation (15). The same simplification

might be possible in the field, if the objects concerned were either non-permeable or permeable with the same μ_r. This might not be too farfetched, because in our application the permeable objects are all made of similar grades of steel. Moreover, for high enough values of μ_r, the values of k_n vary slowly with μ_r as can be seen from Table 2.

With this background, a nonlinear fitting algorithm was used to fit and extract parameters from simulated data typical of our application. The types of fit obtained in three test cases along with the estimates of the parameters are shown in Figs. 27, 28, 29. Additional results are shown in Table 3. Even though reasonably good fits were obtained in most cases, the accuracy of the estimates of parameters were, as expected for the functions involved, very much dependent on the knowledge of the actual number of significant exponential terms in the signal. Thus, in practice, either a number of values of NT should be tried to fit unknown data or a reliable means of ascertaining the inherent number of significant exponentials should be applied. These aspects will be investigated in the future.

B. Prony's Method: This method [19] has been used with some degree of success in underwater acoustics and electromagnetics, where waveforms involved contain a series of damped complex exponentials. The performance of this method on data containing only damped real exponentials has not been evaluated to the same degree. It was recognized, at the beginning, that accurate estimation of the decay factors is difficult in the case of damped real exponentials which are highly correlated. Prony's method can be briefly described as follows:

Given uniformly spaced (ΔT) samples of a waveform

$$u_i \equiv u(t_i) = \sum_{j=1}^{N} A_j e^{-\alpha_j (i\Delta T)}, \quad i = 0, 1, 2, \ldots\ldots M-1 \qquad (22)$$

the algorithm consists of first solving a linear system of equations

of the form

$$\sum_{p=0}^{N-1} a_p u_{p+i} = -u_{N+i}, \quad i = 0, 1, 2, \ldots\ldots\ldots\ldots M - N-1 \qquad (23)$$

to obtain estimates of the coefficient a_p's. Let us denote these as $\bar{a}_p$. Next a polynomial of the form,

$$Z^N + \bar{a}_{N-1} Z^{N-1} + \ldots\ldots\ldots\ldots\ldots + \bar{a}_1 Z + \bar{a}_o = 0 \qquad (24)$$

is solved for its roots $\bar{Z}_j$ where $\bar{Z}_j = e^{-\bar{\alpha}_j \Delta T}$ (25)

The estimates of decay constants, $\bar{\alpha}_j$, are then determined from

$$\bar{\alpha}_j = -\frac{1}{\Delta T} \text{Ln } \bar{Z}_j$$

Once the $\bar{\alpha}_j$'s are found the $\bar{A}_j$'s can be found from the solution of a linear system of equations. Since Prony's method is basically a nonlinear fitting procedure where the nonlinearity of the system is concentrated in a single polynomial, most of the general comments made with regard to nonlinear fitting are applicable to Prony's method. One advantage of Prony's method over standard nonlinear fitting is that one does not need an initial guess of the parameters. As a first attempt, we investigated this method only for the case where M = 2N, i.e. the number of sample points used was exactly twice the assumed number of exponentials in the waveform. This results in linear systems that can be uniquely solved for the $\bar{a}_p$'s and $\bar{A}_j$'s.

Redundancy obtainable from additional samples and least squares solutions of overdetermined systems of equations might be required to make the method viable in case of noisy data.

Results obtained for decay constants in some representative test cases are shown in Table 4. In the cases shown, the parameters α_j were quite accurately estimated provided:

1. The number of exponentials, N, in the waveform was known.

2. The sampling interval, ΔT, was properly chosen.

3. The signal to noise, S/N, ratio was adequate.

A detailed evaluation of all these factors has not been carried out yet. However, the following observations were made from the cases tried. A lack of knowledge of N resulted in either inaccurate or complex values of the $\overline{\alpha}_j$'s or in negative real roots, $\overline{Z}_j$, of the polynomial (24). Too small a sample interval, ΔT, produced roots, $\overline{Z}_j$, very close to each other, making the solution of (23) and (24) unstable. It was noticed that a sampling interval, ΔT, of the order of twice the lowest time constant to be resolved, was often a good choice. A sampling interval much lower than this resulted in numerical instability. This interesting aspect of Prony's method was found extremely sensitive to noise. Since the signal amplitude decays rapidly with time resulting in rapidly decreasing S/N ratio, the degrading effect of noise will overcome the benefits of sampling at widely separated times. For a given N, a compromise between ΔT and S/N ratio has to be found.

In summary, if a favourable S/N ratio could be obtained in the laboratory, Prony's method might be applied with a suitable sampling interval to obtain estimates of the decay factors to determine their dependence on shape and orientation of the object.

C. Profile Matching Methods: Since there does not appear to be any simple and quick way of extracting object parameters from the waveforms, attention was turned to methods of comparing an unknown waveform with a catalogue of stored known waveforms. An efficient method of achieving this must first represent the waveform with a small number of features. No analysis of various feature sets for the waveforms concerned was made. Instead, a set of features was chosen intuitively based on the following argument: A sum of exponentials can be thought of as an equivalent single exponential which has a time-varying decay constant. It was argued that due to the high

correlation between damped exponentials, it should be possible to fit single exponentials to small enough segments of the waveforms. A waveform normalized at t = 0 was thus broken into P segments of 50 μS each and a single exponential was fitted to each segment to estimate an 'equivalent decay factor' for that interval. The collection of these decay factors representing the waveform during the various time segments was taken as the feature set to describe the waveform. Except for very small times (the first 50 μS) for small objects, good fits were obtained in all representative cases. Two samples are shown in Figs. 30 and 31. The uncertainty in the estimates of the parameters increase as we approach the noisy tails of the waveforms.

Another feature selection scheme which seems natural to signals which are sums of damped exponentials is the use of a complete set of orthogonal exponentials to approximate the waveforms [20]. One foreseeable problem with this method is the choice of an appropriate small set of decay constants that would approximate waveforms which have a wide range of decay rates. This is the case for the application at hand. Preliminary investigation of this aspect has been initiated.

Feature vectors employing the former scheme were calculated for a total of 18 equivalent spheres representing 9 rounds ranging from 20 mm to 155 mm and Steel, Al and Cu spheres ranging in diameter from 2.54 to 7.62 cm from computer simulated responses with added Gaussian noise (Table 5). The known set of feature vectors (also called the design set [27] was obtained from responses simulated with noise of standard deviation $\sigma_R = 0.001$, which corresponds to a signal to noise amplitude ratio of 1000:1 at the signal maximum (t = 0). This quality of data is thought to be achievable for the design set which could be gathered under laboratory conditions where a large number of responses of an object could be averaged. Two unknown sets of feature vectors (also called test sets) were generated from responses with Gaussian noise of standard deviation, $\sigma_u = 0.005$

and 0.01 respectively. As a preliminary effort, the following classification scheme was applied to the above design and test sets. Each unknown feature vector was compared with all of the stored known feature vectors by calculating the weighted distance as defined below:

$$d_{ij} = \frac{\sum_{k=1}^{P} (\tau^U_{jk} - \tau^R_{ik})^2/(\sigma^2_{R_{ik}} + \sigma^2_{U_{jk}})}{\sum_{k=1}^{P} \frac{1}{(\sigma^2_{R_{ik}} + \sigma^2_{U_{jk}})}} \qquad (27)$$

where

d_{ij} = weighted distance in parameter space between i^{th} stored signature and the j^{th} unknown signature

τ^R_{ik} = the k^{th} time constant of the i^{th} stored signature

τ^U_{jk} = the k^{th} time constant of the j^{th} unknown signature

$\sigma^2_{R_{ik}}$, $\sigma^2_{U_{jk}}$ = variances of τ^R_{ik} and τ^U_{jk} respectively

P = number of time constants (extracted from the first P segments of the waveforms) used in calculating d_{ij}.

An unknown object, j, was then associated with that known object, i, whose feature vector was the closest to that of the unknown, i.e. minimum d_{ij} for all i. This experiment was repeated 20 times with a new set of unknown responses simulated with different noise samples for each selected noise variance. Also for each case the number of features used, P, was varied. The results of these trials for various P's and σ_U's are summarized in the form of "confusion matrices" in Tables 6(a) to 6(j) and 7(a) to 7(j). In these tables the objects are arranged in decreasing order of their response parameters, i.e. the product "$\mu\sigma a^2$". The entry in the j^{th} row and i^{th} column denotes the number of times out of 20 trials, the j^{th} unknown

object was classified as the i^{th} known object. An empty space in the tables represents a zero.

It must be emphasized that these results are only exploratory and should not be used to reach a conclusion as to the practicality of a profile-matching technique. However, the following observations can be made from the results, which should be utilized in future work.

(1) For a given noise variance σ_U^2, the performance of the classifier first improves and then deteriorates with increasing number of parameters used - suggesting a range of optimum values for P for the given trials. Although the optimum range seems to be 5 to 7 for the trials, the choice of P has to be made from performance of the method on measured data.

(2) As is obviously expected, the overall performance of the method is better for lower noise variances for a given number of parameters.

(3) The less than ideal performance for objects 2, 3 and 4 may be attributed to the fact that they have the same permeability and conductivity and differ only a small amount in radius, though not enough in the presence of noise to always identify them correctly. Discrimination between 17 and 18 gets worse with increasing number of parameters. This is to be expected because their response parameters are relatively small and hence the effect of noise predominates after a shorter period of time. These observations point to the fact that for a given noise level, restrictions have to be established by measurements on identifiable differences between objects. Also, the number of parameters used may have to be different for different objects.

In addition, a conclusion as to the practicality of the profile-matching technique in range clearance must await the completion of the investigation of at least the following aspects:

(1) Performance of profile-matching schemes with measured responses for different positions and orientations of actual shells (whose electrical properties are expected to vary even among the same type) with respect to the sensor, geometry has to be evaluated.

(2) Effect of actual noise and the number of parameters used in a particular scheme must be determined to establish limits of performance.

(3) Typical shrapnel types should be included in the test to ascertain the probability of their being misclassified as a shell.

(4) Performance of other feature selection and classification schemes should be investigated possibly incorporating the concept of unequal frequency of occurence of a shell and shrapnel. In such a scheme, more penalty for misclassifying a shell as a piece of shrapnel would be assessed than for misclassifying a piece of shrapnel as a shell.

IV. SUMMARY

This paper has explored two potential short term methods for the detection of buried ordnance, namely magnetometer and electromagnetic induction techniques.

It has been demonstrated that magnetometers can be used to accurately determine depth and location of buried ferrous ordnance and the orientation and magnitude of the associated dipole moment in pseudo-real-time. It was shown that there are fundamental difficulties associated with determining object size and based on the knowledge of the orientation and magnitude of the dipole moment further experimentation is required to determine the extent of these difficulties.

Electromagnetic induction was shown to be capable of determining the depth and location of ferrous and nonferrous ordnance in at least pseudo-realtime. The question of determination of size and electromagnetic properties of the object from its electromagnetic pulse induction signature was extensively studied. It was found that explicit determination of the above properties is difficult, if not impossible. Methods of object classification based on stored signatures were investigated as a possible alternative. The feasibility of such methods will only be known following further experimental studies.

It should be emphasized that both methods are complementary. It is envisioned that future range clearance systems would consist of both detector types to ensure more reliable detection and identification.

REFERENCES

[1] G.F. Greco, B.W. Springfield and W.E. Main, Contaminated Area Clearance and Land-Use Alternatives, pp. C11-C13, Engineer Studies Group Office, Chief of Engineers Department of the Army United States Report ADB002767, January 1975.

[2] F. Grant and G. West, Interpretation Theory in Applied Geophysics pp. 306-381, New York: McGraw-Hill, 1965.

[3] S. Breiner, Applications Manual for Portable Magnetometers, Sunnyvale, California: GeoMetrics, Inc., 1973.

[4] P. Lorrain and D. Corson, Electromagnetic Fields and Waves, pp. 319-321, San Francisco: W.H. Freeman, 1970.

[5] K. Whitham, "Measurement of the Geomagnetic Elements", Methods and Techniques in Geophysics, S. Runcorn, ed. pp. 104-167, New York: Interscience, 1960.

[6] F. Primdahl, "The Fluxgate Magnetometer", J. Phys. E: Sci. Instrum. 12., pp. 241-253, 1979.

[7] C. Falco, "SQUIDS: Applications Outside the Laboratory", Physics in Technology 9, pp. 148-153, 1978.

[8] S. Parker Gay Jr., "Standard Curves for Interpretation of Magnetic Anomalies over Long Tabular Bodies", Mining Geophysics, pp. 512-548, Tulsa, Oklahoma: The Society of Exploration Geophysicists, 1967.

[9] R. Henderson and I. Zietz, "Polar Charts for Calculating Aeromagnetic Anomalies of Three-Dimensional Bodies", Mining Geophysics, pp. 554-568, Tulsa, Oklahoma: The Society of Exploration Geophysicists, 1967.

[10] D. Lemercier and A. Salvei, "Method and Device for Determining the Depth of a Magnetic Anomaly", Canadian Patent No. 960305, December 1974.

[11] R. Henderson and I. Zietz, "Magnetic-Doublet Theory in Analysis of Total Intensity Anomalies", Mining Geophysics, pp. 490-511, Tulsa, Oklahoma: The Society of Exploration Geophysicists, 1967.

[12] A. McAulay "Computerized Model Demonstrating Magnetic Submarine Location", IEEE Trans Aerospace and Electronic Systems Vol. AES-13, pp. 246-254, May 1977.

[13] W. Wynn, C. Frahm, P. Carroll, R. Clark, J. Wellhoner and M. Wynn, "Advanced Superconducting Gradiometer/Magnetometer Arrays and a Novel Signal Processing Technique", IEEE Trans. Mag. Vol. MAG-11, pp. 701-707, March 1975.

REFERENCES (Cont'd)

[14] D. Smellie, "Elementary Approximations in Aeromagnetic Interpretation", Mining Geophysics, pp. 474-480, Tulsa, Oklahoma: The Society of Exploration Geophysicists, 1967.

[15] D. Marquardt, "An Algorithm for Least-Squares Estimation of Nonlinear Parameters", J. Soc. Ind. Appl. Math. 11, pp. 431-441, 1963.

[16] R. Fletcher and M. Powell, "A Rapidly Convergent Descent Method for Minimization" The Computer Journal 6, pp. 163-168, 1963.

[17] P. Bevington, Data Reduction and Error Analysis for the Physical Sciences, pp. 204-246, New York: McGraw-Hill, 1969.

[18] R. Kemp, A Theoretical Report for Pulsed Eddy Current Metal Detector, Plessy Company Limited, U.K., March 1970.

[19] F.B. Hildebrand, Introduction to Numerical Analysis, pp. 378-382, New York: McGraw-Hill, 1956.

[20] W.H. Huggins, Representation and Analysis of Signals - Part I - The use of Orthogonalized Exponentials, AFCRC-TR-57-357, AD133741, 1958.

[21] P. Chestnut, H. Landsman and R.W. Floyd, "A Sonar Target Recognition Experiment", J. Acoust. Soc. Am. Vol. 66, pp. 140-147, July 1979.

[22] J. Stratton, "Electromagnetic Theory", pp. 207-217 and 258, New York: McGraw-Hill, 1941.

[23] J. Jacobs, "The Earth's Magnetic Field", Mining Geophysics, pp. 424-436, Tulsa, Oklahoma: The Society of Exploration Geophysicists, 1967.

APPENDIX A

DERIVATION OF THE EQUATIONS OF THE MAGNETIC DIPOLE MOMENT INDUCED IN A PERMEABLE SPHEROID BY AN AMBIENT MAGNETOSTATIC FIELD

APPENDIX A

DERIVATION OF THE EQUATIONS OF THE MAGNETIC DIPOLE MOMENT INDUCED IN A PERMEABLE SPHEROID BY AN AMBIENT MAGNETOSTATIC FIELD

The shapes of artillery shells are complex and are not governed by simple equations. One might, however, as a reasonable first approximation, choose to model such objects by prolate spheroids. Although clearly not completely accurate, such a model will serve to demonstrate how size can be extracted from the dipole parameters. Consider a uniform ferrous spheroid and choose a spherical polar coordinate system (Fig. 3) such that the components of the ambient magnetostatic field are $(H_0, \theta_0, 0)$. The component, $\vec{H}_{03}$, of the ambient field along the major $(\hat{3})$ axis of the spheroid is given by

$$\vec{H}_{03} = (H_{03}, \theta_3, \phi_3) \tag{A-1}$$

and we define a vector $\vec{H}_{012}$ orthogonal to $\vec{H}_{03}$ such that

$$\vec{H}_0 = \vec{H}_{03} + \vec{H}_{012} \tag{A-2}$$

$$\vec{H}_{012} = (H_{012}, \theta_{12}, \phi_{12})$$

The induced magnetic moment of the spheroid may be derived from the equations for the magnetic field in the spheroid [22] and is given by

$$\vec{M} = V\vec{m} = \frac{4}{3}\pi a^2 c \left[\frac{(\mu_1/\mu_0) - 1}{1 + \frac{a^2 c}{2\mu_2}(\mu_1 - \mu_2)A_3} \vec{H}_{03} + \frac{(\mu_1/\mu_0) - 1}{1 + \frac{a^2 c}{2\mu_2}(\mu_1 - \mu_2)A_{12}} \vec{H}_{012} \right] \tag{A-3}$$

where $\vec{m}$ is the dipole moment per unit volume

V is the volume of the spheroid

a is the length of the semiminor axis of the spheroid

c is the length of the semimajor axis of the spheroid

μ_0 is the permeability of free space

μ_1 is the permeability of the spheroid

μ_2 is the permeability of the medium surrounding the object (usually = μ_0)

$$\text{and } a^2cA_3 = \frac{-2e}{e^2-1}\left(\frac{1}{e} + \frac{1}{(e^2-1)^{1/2}} \text{Ln } (e - (e^2 - 1)^{1/2})\right)$$

$$a^2cA_{12} = \frac{e}{e^2-1}\left(e + \frac{1}{(e^2-1)^{1/2}} \text{Ln } (e - (e^2 - 1)^{1/2})\right) \qquad \text{(A-4)}$$

$$e = c/a > 1$$

Values for the components $\vec{H}_{03}$ and $\vec{H}_{012}$ may be readily obtained by calculation of the applicable scalar products:

$$H_{03} = H_0(\text{Cos } \theta_0 \text{ Cos } \theta_3 + \text{Sin } \theta_0 \text{ Sin } \theta_3 \text{ Cos } \phi_3)$$

$$H_{012}^2 = H_0^2 - H_{03}^2 \qquad \text{(A-5)}$$

$$\text{Cos } \theta_{12} = \frac{H_0}{H_{012}} \text{Sin } \theta_3 \text{ (Cos } \theta_0 \text{ Sin } \theta_3 - \text{Sin } \theta_0 \text{ Cos } \theta_3 \text{ Cos } \phi_3)$$

$$\phi_{12} = \phi_3 - \text{Cos}^{-1}\left(\frac{-1}{\text{Tan } \theta_3 \text{ Tan } \theta_{12}}\right)$$

Thus, by use of equations (A-3) to (A-5) we can calculate the components of $\vec{m}$ (m, β, ϕ_m) as a function of θ_3, ϕ_3. These are plotted in Figures 4, 5, 6 for $\mu_1 = 51\ \mu_0$, a = 0.05 m, c = 0.20 m, $\theta_0 = 17°$ and $\mu_0 H_0 = 60000$ nT which are typical values for medium size howitzer shells at latitudes similar to those of many Canadian artillery ranges. Since $\vec{M}$ is directly proportional to $\vec{H}_{03}$ and $\vec{H}_{012}$ and even during magnetic storms, H_0 does not vary by more than about 0.2% [3], [23], a given class of spheroids (constant mass density, μ_1, e) should have the same family of curves for a constant geographical location. It should then be possible from values of M, β and α ($\alpha = \phi_B - \phi_m + \pi/2$ where ϕ_B is the known traverse bearing angle) determined by the nonlinear fit, (Section II) to determine $\vec{m}$ and hence the volume or mass of the spheroid. Clearly the curves indicate that a finite probability exists of obtaining multiple mass values and this probability increases as desired resolution in mass increases. Further, if additional significantly different classes of spheroids are expected to be

encountered, extra sets of curves must be employed thereby increasing the probability of obtaining multiple mass values. The same rationale applies to the different shaped shells that might be found on an artillery range. In this case, the curves for each shell type would be found empirically prior to employing the detector array. There would generally be about ten different types of shells and knowledge of mass would be required to within about 25%. Only actual experiments would show if it were feasible to extract mass, volume and body orientation from M, β and α for a given type of problem.

APPENDIX B

DERIVATION OF THE CARTESIAN AND TOTAL FIELD COMPONENTS OF A MAGNETIC DIPOLE

APPENDIX B

DERIVATION OF THE CARTESIAN AND TOTAL FIELD COMPONENTS OF A MAGNETIC DIPOLE

Consider a magnetic dipole with body fixed spherical polar coordinates given by (1) using the geometry of Figure 7. We define a cartesian coordinate system whose origin coincides with the dipole location, such that the dipole axis forms an angle, β, with respect to the z axis and lies in the xz plane. The cartesian components, (H_x, H_y, H_z), are related to the spherical polar coordinates by the 3 × 3 matrix of inner products

$$\begin{bmatrix} H_x \\ H_y \\ H_z \end{bmatrix} = \begin{bmatrix} \hat{x}.\hat{r} & \hat{z}.\hat{\theta} & \hat{x}.\hat{\phi} \\ \hat{y}.\hat{r} & \hat{y}.\hat{\theta} & \hat{y}.\hat{\phi} \\ \hat{z}.\hat{r} & \hat{z}.\hat{\theta} & \hat{z}.\hat{\phi} \end{bmatrix} \begin{bmatrix} H_r \\ H_\theta \\ H_\phi \end{bmatrix} \qquad \text{(B-1)}$$

Only six elements of the matrix of inner products are required since $H_\phi = 0$. Using geometrical construction, we find that we can define two additional angles, Ψ and γ, to yield three cosine relationships

$$\begin{aligned} \text{Cos}\theta &= (z\text{Cos}\,\beta - x\text{Sin}\,\beta)/r \\ \text{Cos}\Psi &= (x + z\text{Tan}\,\beta)/(y^2 + (x + z\text{Tan}\,\beta)^2)^{1/2} \\ \text{Cos}\gamma &= -\text{Cos}\Psi\,\text{Sin}\beta \end{aligned} \qquad \text{(B-2)}$$

The necessary inner products can be then written as

$$\begin{aligned} \hat{x}.\hat{r} &= x/r \\ \hat{x}.\hat{\theta} &= \text{Cos}\Psi/\text{Sin}\,(\gamma-\theta) - x/(r\text{Tan}\,(\gamma-\theta)) \\ \hat{y}.\hat{r} &= y/r \\ \hat{y}.\hat{\theta} &= \text{Sin}\Psi/\text{Sin}\,(\gamma-\theta) - y/(r\text{Tan}\,(\gamma-\theta)) \\ \hat{z}.\hat{r} &= z/r \\ \hat{z}.\hat{\theta} &= -z/(r\text{Tan}\,(\gamma-\theta)) \end{aligned} \qquad \text{(B-3)}$$

Tedious substitution and simplification lead to equations (2) and (3).

The total magnetic field, $\vec{H}_T$, is defined by

$$\vec{H}_T = \vec{H}_o + \vec{H} \tag{B-4}$$

High precision total field instruments measure only the magnitude of the magnetic field, $H_T = |\vec{H}_T|$, and not its direction. The magnitude is given by

$$H_T = (H_o^2 + H^2 + 2\vec{H}_o \cdot \vec{H})^{1/2} \tag{B-5}$$

where $H_o = |\vec{H}_o|$ and $H = |\vec{H}|$ as in equation (3).

If we expand (B-5) using a Taylor expansion to second order we get

$$H_T = H \, \mathrm{Cos}\theta_{AD} + \frac{H^2}{2H_o} \mathrm{Sin}^2\theta_{AD} + H_o \tag{B-6}$$

where θ_{AD} is the angle between the ambient and dipole field directions. In geophysical studies, it is common to omit the second (second order) term on the right hand side of (B-6). For our use, substitution shows that such an omission can lead to errors of 1 nT for a 250 nT anomaly in certain orientations, which could be significant.

We define θ_o and $\phi_o = \phi_m - \pi$ (ϕ_m is defined in Appendix A) as the polar and azimuthal angles of the earth's field with respect to the z- and x-axes respectively of the dipole. Geometrical construction easily shows that

$$\mathrm{Cos}\theta_{AD} = \frac{H_x \mathrm{Sin}\theta_o \mathrm{Cos}\phi_o + H_y \mathrm{Sin}\theta_o \mathrm{Sin}\phi_o + H_z \mathrm{Cos}\theta_o}{(H_x^2 + H_y^2 + H_z^2)^{1/2}} \tag{B-7}$$

Substitution of (B-7) into (B-6) leads to (3).

The advantage of equation (4) is that H_o and hence H_T are orders of magnitude greater than H and thus baseline subtraction of H_o from equation (4) yields an expression whose value is much more sensitive to the magnetic anomaly than the total field value unaltered.

TABLE 1 (Cont'd)

Object Type	Orientation θ_3(°)	Orientation ϕ_3(°)	Depth of Center of Mass (z in m) (±0.01)	Estimated Dipole Center Depth (m)	Reduced χ^2 of Fit (r.m.s. data uncertainty = 3 nT)
105 mm shrapnel intact but hollowed out	0	-	0.70	0.641±0.002	1.2
	90	90	0.70	0.713±0.009	0.6
	90	135	0.70	0.766±0.010	0.4
	90	180	0.70	0.709±0.007	0.3
	45	90	0.70	0.679±0.002	0.6
	45	135	0.70	0.702±0.003	1.0
	45	180	0.70	0.697±0.002	0.3
shrapnel[2]	-	-	0.60	0.566±4.011	22.8[1]
shrapnel[2 3]	-	-	0.60	0.493±0.105	0.6
shrapnel[2]	-	-	0.60	0.634±0.005	1.0
shrapnel[2 3]	-	-	0.60	0.465±0.025	0.5
shrapnel[2 3]	-	-	0.60	0.891±0.050	0.7

[1] Data values in excess of 750 nT

[2] Shrapnel are very irregular shapes and range in mass from 1 to 8 kg

[3] Very low maximum signal to noise (~ 8 - 15)

TABLE 1

CALCULATED AND MEASURED
OBJECT DEPTHS

Object Type	Orientation $\theta_3(^\circ)$	Orientation $\phi_3(^\circ)$	Depth of Center of Mass (z in m) (±0.01)	Estimated Dipole Center Depth (m)	Reduced χ^2 of Fit (r.m.s. data uncertainty = 3 nT)
105 mm shell dummy round 14.3 kg	0	-	0.70	0.649±0.004	14.9[1]
			0.95	0.913±0.005	2.3[1]
			1.45	1.445±0.012	0.7
105 mm shell	90	90	0.70	0.677±0.004	0.5
			0.95	0.907±0.015	0.7
			1.45	1.565±0.058	0.4
105 mm shell	90	135	0.70	0.703±0.003	0.4
			0.95	0.915±0.011	0,6
			1.45	1.907±0.001	0.3
105 mm shell	90	180	0.70	0.721±0.005	0.7
			0.95	0.944±0.014	0.7
			1.45	1.408±0.044	0.3
105 mm shell	45	90	0.70	0.677±0.002	0.6
			0.95	0.948±0.006	0.6
			1.45	1.555±0.023	0.3
105 mm shell	45	135	0.70	0.671±0.002	0.7
			0.95	0.927±0.005	0.6
			1.45	1.552±0.020	0.3
105 mm shell	45	180	0.70	0.681±0.002	2.6[1]
			0.95	0.940±0.003	0.6
			1.45	1.458±0.004	0.6

TABLE 3
ADDITIONAL RESULTS FOR NON-LINEAR FITTING
OF SIMULATED DATA

Data (t_i=1,2,...256)	Ratio of Signal amplitude at t=0 to noise St. Dev	Fitting Function and Initial Guesses	Extracted Parameters	Remark
$U(t_i)=2e^{-0.001t_i}+4e^{-0.004t_i}+9e^{-0.009t_i}$	1500	$y(t)=A_1e^{-B_1t}+A_2e^{-B_2t}+A_3e^{-B_3t}$ Initial guesses for B_1, B_2, B_3 were exact values of them, i.e. 0.001, 0.004, 0.009 respectively. Guesses for A_1, A_2, A_3 were 1.9, 3.8, 9.3 respectively.	$\overline{A}_1$=1.92±0.01 $\overline{B}_1$=0.00099±.00002 $\overline{A}_2$=3.82±0.01 $\overline{B}_2$=0.00377±0.00003 $\overline{A}_3$=9.26±.01 $\overline{B}_3$=0.00893±.00001	Good fit obtained. Good estimate of parameters.
$U(t_i)=2e^{-0.001t_i}+4e^{-0.004t_i}+9e^{-0.009t_i}$	100	$y(t)=A_1e^{-B_1t}+A_2e^{-B_2t}+A_3e^{-B_3t}$ Initial guesses for B_1, B_2, B_3 were exact values of them, i.e. 0.001, 0.004, 0.009 respectively. Guesses for A_1, A_2, A_3 were 1.9, 3.8, 9.3 respectively.	$\overline{A}_1$=1.94±0.30 $\overline{B}_1$=0.0013±0.0007 $\overline{A}_2$=3.83±0.37 $\overline{B}_2$=0.0035±0.0008 $\overline{A}_3$=9.27±0.40 $\overline{B}_3$=0.0091±0.0003	Good fit obtained. Reasonable estimate of parameters. Effect of increased noise is greater uncertainty in parameters.

UNCLASSIFIED

TABLE 3
(Continued)

Data (t_i=1,2,...256)	Ratio of Signal amplitude at t=0 to noise St. Dev	Fitting Function and Initial Guesses	Extracted Parameters	Remark
$U(t_i)=2e^{-0.001t_i}+4e^{-0.004t_i}+9e^{-0.009t_i}$	100	$y(t)=A_1e^{-B_1t}+A_2e^{-B_2t}+A_3e^{-B_3t}$ Initial guesses for B_1, B_2, B_3 were 0.005, 0.01 and 0.015; for A_1, A_2, A_3 were 3, 6, 10.	$\overline{A}_1$=2.59±0.30 $\overline{B}_1$=0.0012±0.0004 $\overline{A}_2$=4.91±0.42 $\overline{B}_2$=0.0053±0.0008 $\overline{A}_3$=7.53±0.43 $\overline{B}_3$=0.0094±0.0005	Good fit obtained. Parameters more uncertain.
$U(t_i)=2e^{-0.001t_i}+4e^{-0.004t_i}+9e^{-0.009t_i}$	10	$y(t)=A_1e^{-B_1t}+A_2e^{-B_2t}+A_3e^{-B_3t}$ Initial guesses for B_1, B_2, B_3 were 0.005, 0.01 and 0.015; for A_1, A_2, A_3 were 3, 6, 10.	$\overline{A}_1$=3±3 $\overline{B}_1$=0.002±0.005 $\overline{A}_2$=4±4 $\overline{B}_2$=0.004±0.007 $\overline{A}_3$=8±4 $\overline{B}_3$=0.010±0.004	Poor estimation of parameters.

UNCLASSIFIED

TABLE 3
(Continued)

Data (t_i=1,2,...256)	Ratio of Signal amplitude at t=0 to noise St. Dev	Fitting Function and Initial Guesses	Extracted Parameters	Remark
$U(t_i)=2e^{-0.001t_i}+4e^{-0.004t_i}+9e^{-0.009t_i}$	10	$y(t)=A_1e^{-B_1t}+A_2e^{-B_2t}+A_3e^{-B_3t}$ Initial guesses for B_1, B_2, B_3 were exact values of them, i.e. 0.001, 0.004, 0.009 respectively. Guesses for A_1, A_2, A_3 were 1.9, 3.8, 9.3 respectively.	A_1=2±4 B_1=0.003±0.011 A_2=4±4 B_2=0.003±0.006 A_3=9±4 B_3=0.010±0.003	Poor estimate of parameters.
$U(t_i)=2e^{-0.001t_i}+4e^{-0.004t_i}+9e^{-0.009t_i}$	1500	$y(t)=A_1e^{-B_1t}+A_2e^{-B_2t}+A_3e^{-B_3t}$ Initial guesses for B_1, B_2, B_3 were 0.005, 0.01 and 0.015; for A_1, A_2, A_3 were 3, 6, 10.	$\overline{A}_1$=2.56±0.02 $\overline{B}_1$=0.00115±0.00003 $\overline{A}_2$=4.94±0.03 $\overline{B}_2$=0.00523±0.00005 $\overline{A}_3$=7.50±0.03 $\overline{B}_3$=0.00937±0.00003	Good fit obtained. But Calculated parameters differ from actual ones. This and the following two examples show the effect of initial guesses.

UNCLASSIFIED

TABLE 4
SOME REPRESENTATIVE RESULTS WITH PRONY'S METHOD

Decay Constants, α_j, present in the data (time in μs)	Ratio of Signal Amplitude at t=0 to noise St. Dev	Sampling Interval (μs) ΔT	Assumed Value of N and M	Extracted decay constants, $\bar{\alpha}_j = -\frac{1}{\Delta T} \text{Ln } \bar{z}_j$	Remark
0.001, 0.004, 0.009	∞	400	N=3, M=6	0.001, 0.004, 0.009	$\bar{\alpha}_j$'s properly recovered
0.001, 0.004, 0.009	∞	200	N=3, M=6	0.001, 0.004, 0.009	$\bar{\alpha}_j$'s properly recovered
0.001, 0.004, 0.009	∞	100	N=3, M=6	0.001, 0.004, 0.009	$\bar{\alpha}_j$'s properly recovered
0.001, 0.004, 0.009	∞	50	N=3, M=6	0.005±i0.0002, -0.0002	$\bar{\alpha}_j$'s are non-physical ΔT too small
0.001, 0.004, 0.009	7500	200	N=3, M=6	0.001, 0.004, 0.009	$\bar{\alpha}_j$'s properly recovered at this noise level
0.001, 0.004, 0.009	750	200	N=3, M=6	0.0006, 0.002, 0.007	$\bar{\alpha}_j$'s are real but inaccurate, probable cause: noise.

UNCLASSIFIED

TABLE 4
(Continued)

Decay Constants, α_j, present in the data (time in μs)	Ratio of Signal Amplitude at t=0 to noise St. Dev	Sampling Interval (μs) ΔT	Assumed Value of N and M	Extracted decay constants, $\bar{\alpha}_j = -\frac{1}{\Delta T} \mathrm{Ln}\, \bar{z}_j$	Remark
0.001, 0.004, 0.009	∞	125	N=4, M=8	0.009±i0.006, -0.003, -0.0014-i0.025	$\bar{\alpha}_j$'s are non-physical. N used is not equal to number of α_j's in data.
0.001, 0.004, 0.009, 0.016	∞	125	N=4, M=8	0.001, 0.004, 0.009, 0.016	$\bar{\alpha}_j$'s properly recovered
0.001, 0.004, 0.009, 0.016	∞	62.5	N=4, M=8	0.018, 0.016± i0.001, -0.0002	Some $\bar{\alpha}_j$'s are non-physical. ΔT too small
0.001, 0.004, 0.009, 0.016	10,000	125	N=4, M=8	0.001, 0.008, 0.014, 0.012-i0.025	Effect of noise
0.001, 0.004, 0.009, 0.016	10,000	50	N=4, M=8	0.001, 0.009, 0.016, 0.034-i0.025	One non-physical $\bar{\alpha}_j$. Properly recovered $\bar{\alpha}_j$'s are more accurate than for ΔT= 125

UNCLASSIFIED

TABLE 4
(Continued)

Decay Constants, α_j, present in the data (time in μs)	Ratio of Signal Amplitude at t=0 to noise St. Dev	Sampling Interval (μs) ΔT	Assumed Value of N and M	Extracted decay constants, $\bar{\alpha}_j = -\frac{1}{\Delta T} \mathrm{Ln}\, \bar{z}_j$	Remark
0.001, 0.004, 0.009, 0.016	∞	125	N=3, M=6	0.001, 0.006, 0.015	Inaccurate $\bar{\alpha}_j$'s Value of N used was less than the number of exponentials in data.
0.001, 0.004, 0.009, 0.016	∞	125	N=5, M=10	0.012, 0.017 0.0009±i0.0002 -0.015-i0.025	2 non-physical $\bar{\alpha}_j$'s Value of N used was more than the number of exponentials in data.

UNCLASSIFIED

TABLE 5

OBJECTS AND THEIR PARAMETERS

Object	Conductivity σ (s/m)	Relative Permeability μ_r	Equivalent Radius a (m)	Response Parameter $\mu\sigma a^2$ (sec)
1. 155 mm Shell	10^7	21	0.1378	5.012
2. 105 mm Shell	10^7	21	0.1077	3.062
3. 3.5" Rocket	10^7	21	0.1039	2.850
4. 4.2" Projectile	10^7	21	0.1001	2.645
5. 81 mm Mortar	10^7	21	0.0778	1.598
6. 60 mm Mortar	10^7	21	0.0576	0.876
7. 40 mm Shell	10^7	21	0.0481	0.611
8. 3" Steel Sphere	10^7	21	0.0381	0.383
9. 66 mm Rocket	3.54×10^7	1	0.0923	0.379
10. 2" Steel Sphere	10^7	21	0.0254	0.170
11. 20 mm Shell	10^7	21	0.0202	0.108
12. 3" Copper Sphere	5.65×10^7	1	0.0381	0.103
13. 3" Aluminum Sphere	3.54×10^7	1	0.0381	0.065
14. 2" Copper Sphere	5.65×10^7	1	0.0254	0.046
15. 1" Steel Sphere	10^7	21	0.0127	0.043
16. 2" Aluminum Sphere	3.54×10^7	1	0.0254	0.029
17. 1" Copper Sphere	5.65×10^7	1	0.0127	0.011
18. 1" Aluminum Sphere	3.54×10^7	1	0.0127	0.007

TABLE 6(a)

CLASSIFICATION RESULTS FOR P=1; σ_R=0.001; σ_u=0.005;
NUMBER OF TRIALS = 20

UNKNOWN OBJECTS \ KNOWN OBJECTS	1	2	3	4	5	6	7	8	9	10	11	12	13	14	15	16	17	18
1	20																	
2		12	7	1														
3		9	8	3														
4		3	9	8														
5					20													
6						20												
7							20											
8								20										
9									20									
10										20								
11											20							
12												20						
13													20					
14														20				
15															20			
16																20		
17																	20	
18																		20

TABLE 6(b)

CLASSIFICATION RESULTS FOR P=2; σ_R=0.001; σ_u=0.005;
NUMBER OF TRIALS = 20

UNKNOWN OBJECTS \ KNOWN OBJECTS	1	2	3	4	5	6	7	8	9	10	11	12	13	14	15	16	17	18
1	20																	
2		14	6															
3		2	10	8														
4		1	8	11														
5					20													
6						20												
7							20											
8								20										
9									20									
10										20								
11											20							
12												20						
13													20					
14														20				
15															20			
16																20		
17																	18	2
18																	5	15

TABLE 6(c)

CLASSIFICATION RESULTS FOR P=3; σ_R=.001; σ_u=.005;
NUMBER OF TRIALS = 20

UNKNOWN OBJECTS \ KNOWN OBJECTS	1	2	3	4	5	6	7	8	9	10	11	12	13	14	15	16	17	18
1	20																	
2		13	7															
3		2	12	6														
4			8	12														
5					20													
6						20												
7							20											
8								20										
9									20									
10										20								
11											20							
12												20						
13													20					
14														20				
15															20			
16																20		
17																	19	1
18																	7	13

TABLE 6(d)

CLASSIFICATION RESULTS FOR P=4; σ_R=.001; σ_u=.005;
NUMBER OF TRIALS = 20

UNKNOWN OBJECTS \ KNOWN OBJECTS	1	2	3	4	5	6	7	8	9	10	11	12	13	14	15	16	17	18
1	20																	
2		15	5															
3			15	5														
4			8	12														
5					20													
6						20												
7							20											
8								20										
9									20									
10										20								
11											20							
12												20						
13													20					
14														20				
15															20			
16																20		
17																	17	3
18																	9	11

TABLE 6(e)

CLASSIFICATION RESULTS FOR P=5; σ_R=0.001; σ_u=.005;
NUMBER OF TRIALS = 20

UNKNOWN OBJECTS \ KNOWN OBJECTS	1	2	3	4	5	6	7	8	9	10	11	12	13	14	15	16	17	18
1	20																	
2		17	3															
3		1	17	2														
4			8	12														
5					20													
6						20												
7							20											
8								20										
9									20									
10										20								
11											20							
12												20						
13													20					
14														20				
15															20			
16																20		
17																	16	4
18																	10	10

TABLE 6(f)

CLASSIFICATION RESULTS FOR P=6; σ_R=.001; σ_u=.005;
NUMBER OF TRIALS = 20

UNKNOWN OBJECTS \ KNOWN OBJECTS	1	2	3	4	5	6	7	8	9	10	11	12	13	14	15	16	17	18
1	20																	
2		18	2															
3		1	16	3														
4			10	10														
5					20													
6						20												
7							20											
8								20										
9									20									
10										20								
11											20							
12												20						
13													20					
14														20				
15															20			
16																20		
17																	15	5
18																	10	10

TABLE 6(g)

CLASSIFICATION RESULTS FOR P=7; σ_R=.001; σ_u=.005;
NUMBER OF TRIALS = 20

UNKNOWN OBJECTS \ KNOWN OBJECTS	1	2	3	4	5	6	7	8	9	10	11	12	13	14	15	16	17	18
1	20																	
2		15	5															
3		1	16	3														
4			8	12														
5					20													
6						20												
7							20											
8								20										
9									20									
10										20								
11											20							
12												20						
13													20					
14														20				
15															20			
16																20		
17																	11	9
18																	10	10

TABLE 6(h)

CLASSIFICATION RESULTS FOR P=8; σ_R=.001; σ_u=.005;
NUMBER OF TRIALS = 20

UNKNOWN OBJECTS \ KNOWN OBJECTS	1	2	3	4	5	6	7	8	9	10	11	12	13	14	15	16	17	18
1	20																	
2		14	6															
3		1	15	4														
4			7	13														
5					20													
6						20												
7							20											
8								20										
9									20									
10										20								
11											20							
12												20						
13													20					
14														20				
15															20			
16																20		
17																	13	7
18																	10	10

TABLE 6(i)

CLASSIFICATION RESULTS FOR P=9; σ_R=.001; σ_u=.005;
NUMBER OF TRIALS = 20

UNKNOWN OBJECTS \ KNOWN OBJECTS	1	2	3	4	5	6	7	8	9	10	11	12	13	14	15	16	17	18
1	20																	
2		15	5															
3		1	16	3														
4			7	13														
5					20													
6						20												
7							20											
8								20										
9									20									
10										20								
11											20							
12												20						
13													20					
14														20				
15															20			
16																20		
17																	14	6
18																	11	9

TABLE 6(j)

CLASSIFICATION RESULTS FOR P=10; σ_R=0.001; σ_u=0.005;
NUMBER OF TRIALS = 20

UNKNOWN OBJECTS \ KNOWN OBJECTS	1	2	3	4	5	6	7	8	9	10	11	12	13	14	15	16	17	18
1	20																	
2		15	5															
3		1	16	3														
4			7	13														
5					20													
6						20												
7							20											
8								20										
9									20									
10										20								
11											20							
12												20						
13													20					
14														20				
15															20			
16																20		
17																1	15	4
18																	11	9

TABLE 7(a)

CLASSIFICATION RESULTS FOR P=1; σ_R=0.001; σ_u=0.01

NUMBER OF TRIALS = 20

UNKNOWN OBJECTS \ KNOWN OBJECTS	1	2	3	4	5	6	7	8	9	10	11	12	13	14	15	16	17	18
1	16	3	0	1														
2		8	7	5														
3		8	7	5														
4		6	9	5														
5					20													
6						20												
7							20											
8								20										
9									20									
10										20								
11											9		11					
12												20						
13											8		12					
14														20				
15															20			
16																20		
17																	20	
18																		20

TABLE 7(b)

CLASSIFICATION RESULTS FOR P=2; σ_R=0.001; σ_u=0.01;
NUMBER OF TRIALS = 20

UNKNOWN OBJECTS \ KNOWN OBJECTS	1	2	3	4	5	6	7	8	9	10	11	12	13	14	15	16	17	18
1	16	2	2															
2		8	10	2														
3		10	7	3														
4		7	8	5														
5					20													
6						20												
7							20											
8								20										
9									20									
10										20								
11											20							
12												20						
13													20					
14														20				
15															20			
16																20		
17																	19	1
18																	5	15

TABLE 7(c)

CLASSIFICATION RESULTS FOR P=3; σ_R=.001; σ_u=0.01;
NUMBER OF TRIALS = 20

UNKNOWN OBJECTS \ KNOWN OBJECTS	1	2	3	4	5	6	7	8	9	10	11	12	13	14	15	16	17	18
1	18	2																
2		8	10	2														
3		9	7	4														
4		5	8	7														
5					20													
6						20												
7							20											
8								20										
9									20									
10										20								
11											20							
12												20						
13													20					
14														20				
15															20			
16																20		
17																	15	5
18																	6	14

TABLE 7(d)

CLASSIFICATION RESULTS FOR P=4; σ_R=.001; σ_u=0.01;
NUMBER OF TRIALS = 20

UNKNOWN OBJECTS \ KNOWN OBJECTS	1	2	3	4	5	6	7	8	9	10	11	12	13	14	15	16	17	18
1	19	1																
2		11	7	2														
3		6	10	4														
4		4	10	6														
5					20													
6						20												
7							20											
8								20										
9									20									
10										20								
11											20							
12												20						
13													20					
14														20				
15															20			
16																20		
17																	16	4
18																	7	13

TABLE 7(e)

CLASSIFICATION RESULTS FOR P=5; σ_R=0.001; σ_u=0.01;
NUMBER OF TRIALS = 20

UNKNOWN OBJECTS \ KNOWN OBJECTS	1	2	3	4	5	6	7	8	9	10	11	12	13	14	15	16	17	18
1	19		1															
2		10	6	4														
3		7	8	5														
4		3	10	7														
5					20													
6						20												
7							20											
8								20										
9									20									
10										20								
11											20							
12												20						
13													20					
14														20				
15															20			
16																20		
17																	15	5
18																	9	11

TABLE 7(f)

CLASSIFICATION RESULTS FOR P=6; σ_R=.001; σ_u=0.01;
NUMBER OF TRIALS = 20

UNKNOWN OBJECTS \ KNOWN OBJECTS	1	2	3	4	5	6	7	8	9	10	11	12	13	14	15	16	17	18
1	20																	
2		10	6	4														
3		5	9	6														
4		1	11	8														
5					20													
6						20												
7							20											
8								20										
9									20									
10										20								
11											20							
12												20						
13													20					
14														20				
15															20			
16																20		
17																	16	4
18																	9	11

TABLE 7(g)

CLASSIFICATION RESULTS FOR P=7; σ_R=0.001; σ_u=0.01;
NUMBER OF TRIALS = 20

UNKNOWN OBJECTS \ KNOWN OBJECTS	1	2	3	4	5	6	7	8	9	10	11	12	13	14	15	16	17	18
1	20																	
2		11	6	3														
3		6	10	4														
4		2	11	7														
5					20													
6						20												
7							20											
8								20										
9									20									
10										20								
11											20							
12												20						
13													20					
14														20				
15															20			
16																20		
17																	17	3
18																	10	10

TABLE 7(h)

CLASSIFICATION RESULTS FOR P=8; σ_R=0.001; σ_u=.01;
NUMBER OF TRIALS = 20

UNKNOWN OBJECTS \ KNOWN OBJECTS	1	2	3	4	5	6	7	8	9	10	11	12	13	14	15	16	17	18
1	20																	
2		11	7	2														
3		10	7	3														
4		2	10	8														
5					20													
6						20												
7							20											
8								20										
9									20									
10										20								
11											20							
12												20						
13													20					
14														20				
15															20			
16																20		
17																	13	7
18																	9	11

TABLE 7(i)

CLASSIFICATION RESULTS FOR P=9; σ_R=0.001; σ_u=.01;
NUMBER OF TRIALS = 20

UNKNOWN OBJECTS \ KNOWN OBJECTS	1	2	3	4	5	6	7	8	9	10	11	12	13	14	15	16	17	18
1	20																	
2		10	9	1														
3		8	9	3														
4		2	11	7														
5					20													
6						20												
7							20											
8								20										
9									20									
10										20								
11											20							
12												20						
13													20					
14														20				
15															20			
16																20		
17																	16	4
18																	11	9

TABLE 7(j)

CLASSIFICATION RESULTS FOR P=10; σ_R=0.001; σ_u=0.01;
NUMBER OF TRIALS = 20

UNKNOWN OBJECTS \ KNOWN OBJECTS	1	2	3	4	5	6	7	8	9	10	11	12	13	14	15	16	17	18
1	20																	
2		9	10	1														
3		9	9	2														
4		1	12	7														
5					20													
6						20												
7							20											
8								20										
9									20									
10										20								
11											20							
12												20						
13													20					
14														20				
15															20			
16																20		
17																	15	5
18																	11	9

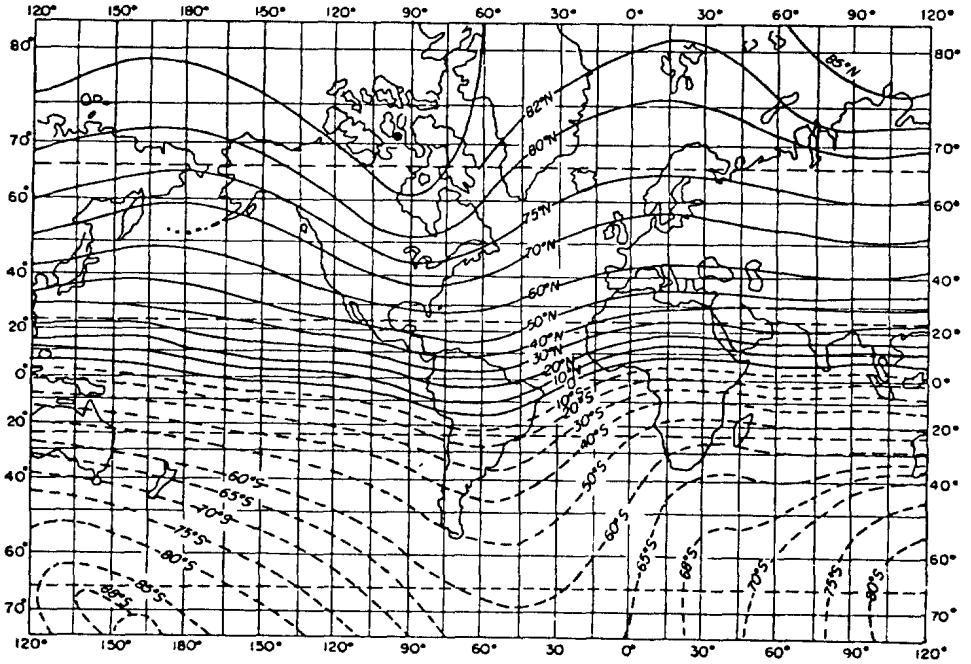

The Geomagnetic Inclination in Degrees of Arc from the Horizontal SOURCE USNHO

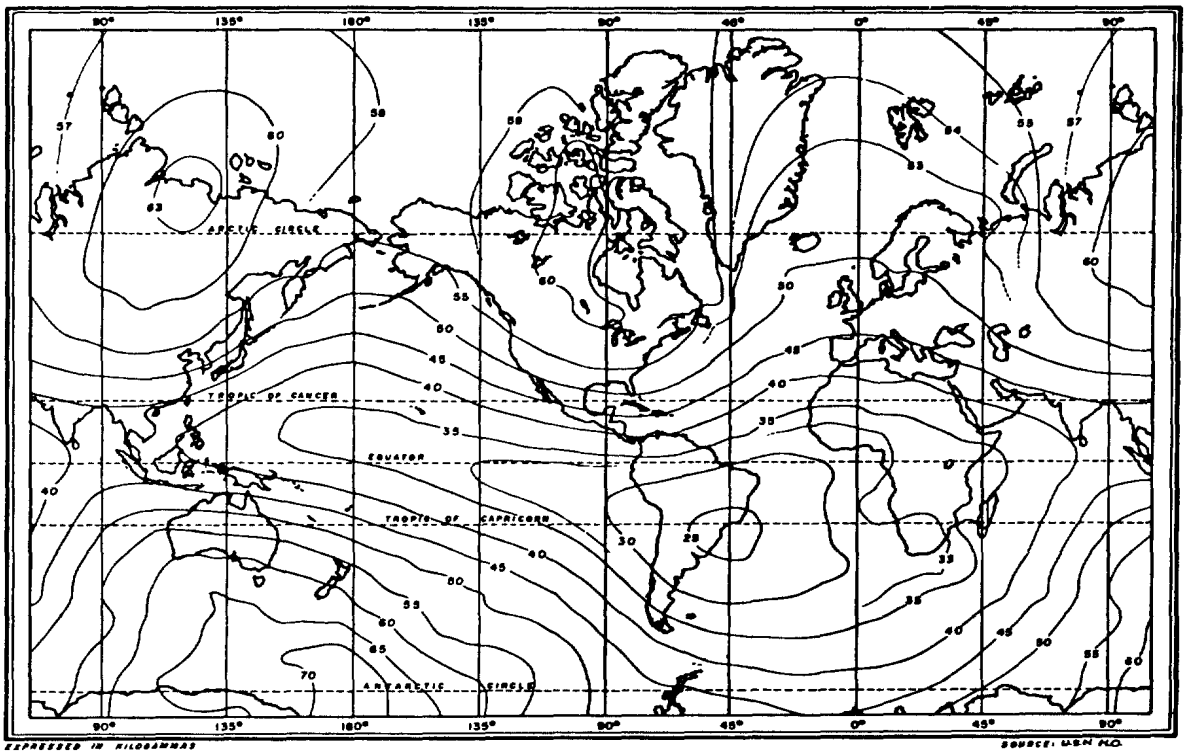

The Total Intensity of the Earth's Magnetic Field

Figure 1

Spatial variation of the earth's magnetic field.
One gamma equals 1 nT. Taken from Ref. 3.

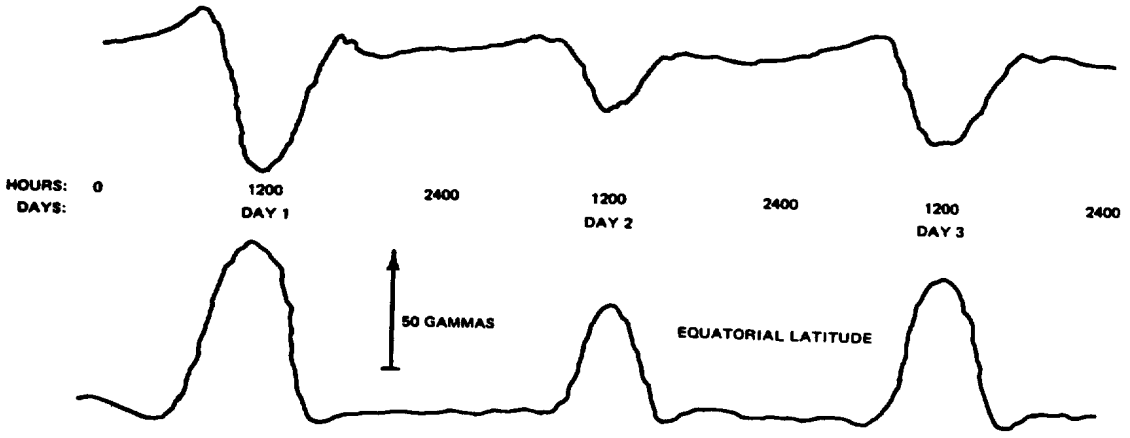

Typical Diurnal Variations in Total Field Intensity

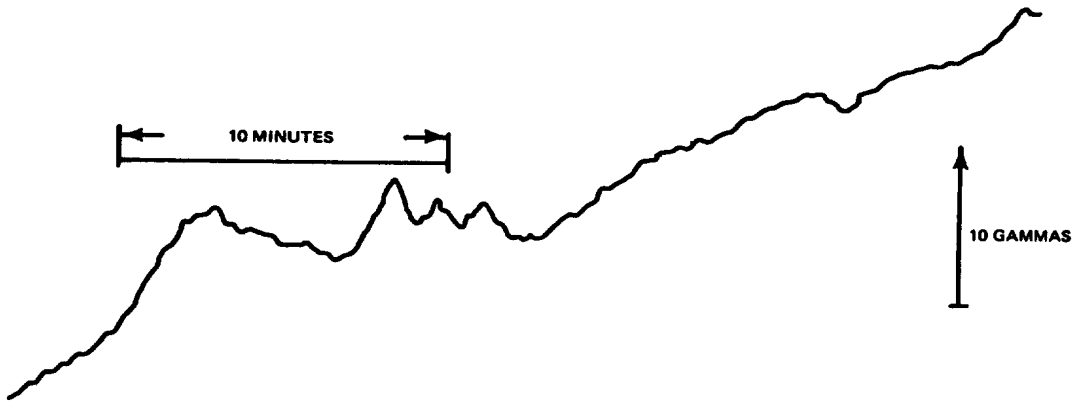

Typical Micropulsations

Typical Magnetic Storm

Figure 2

Temporal variations of the earth's magnetic field.
One gamma equals 1 nT. Taken from Ref. 3.

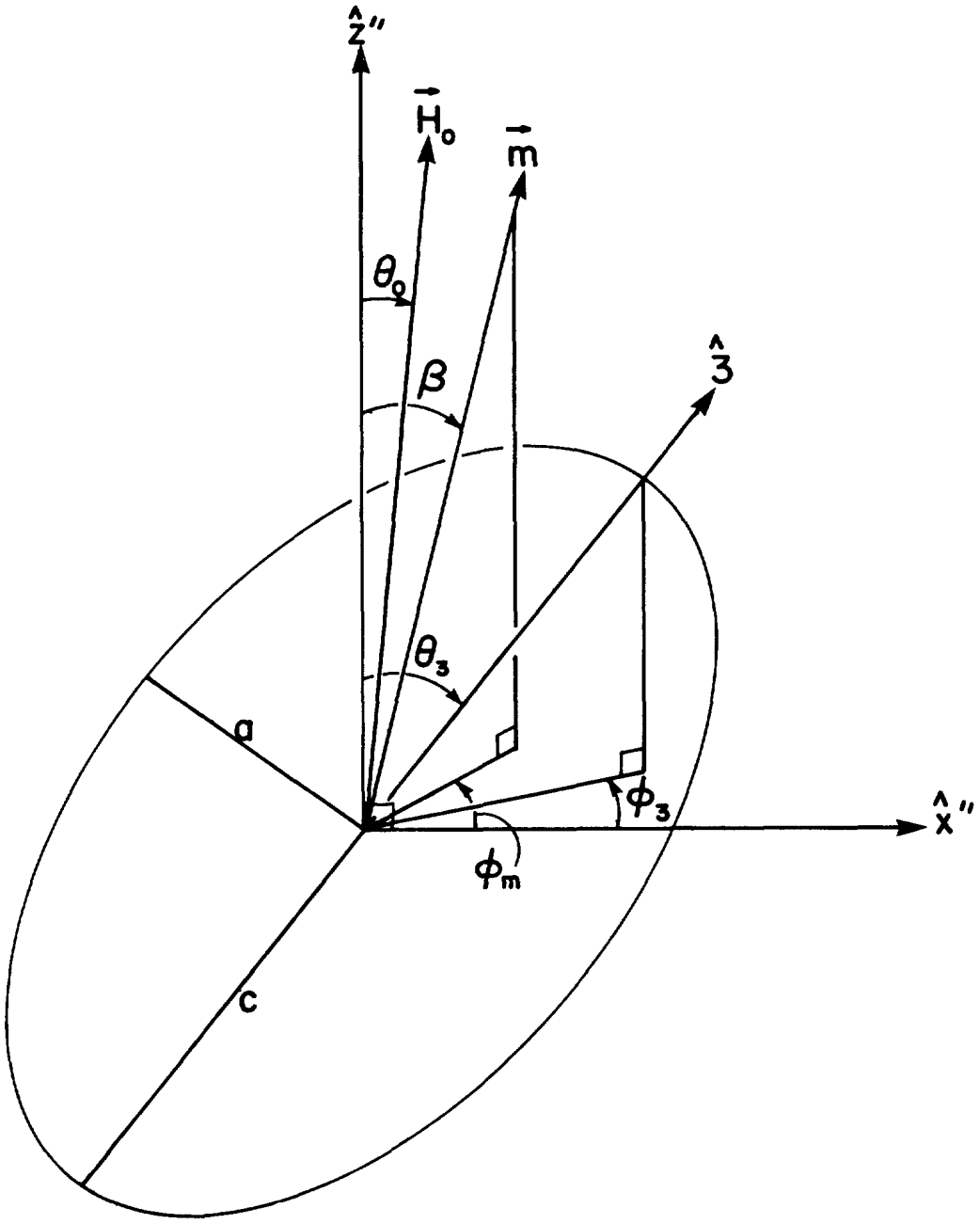

Figure 3

Geometry for calculation of the magnetic moment induced in a spheroid. The ambient magnetic field, $\vec{H}_o$, lies in the $\hat{z}''$ - $\hat{x}''$ plane. See Appendix A.

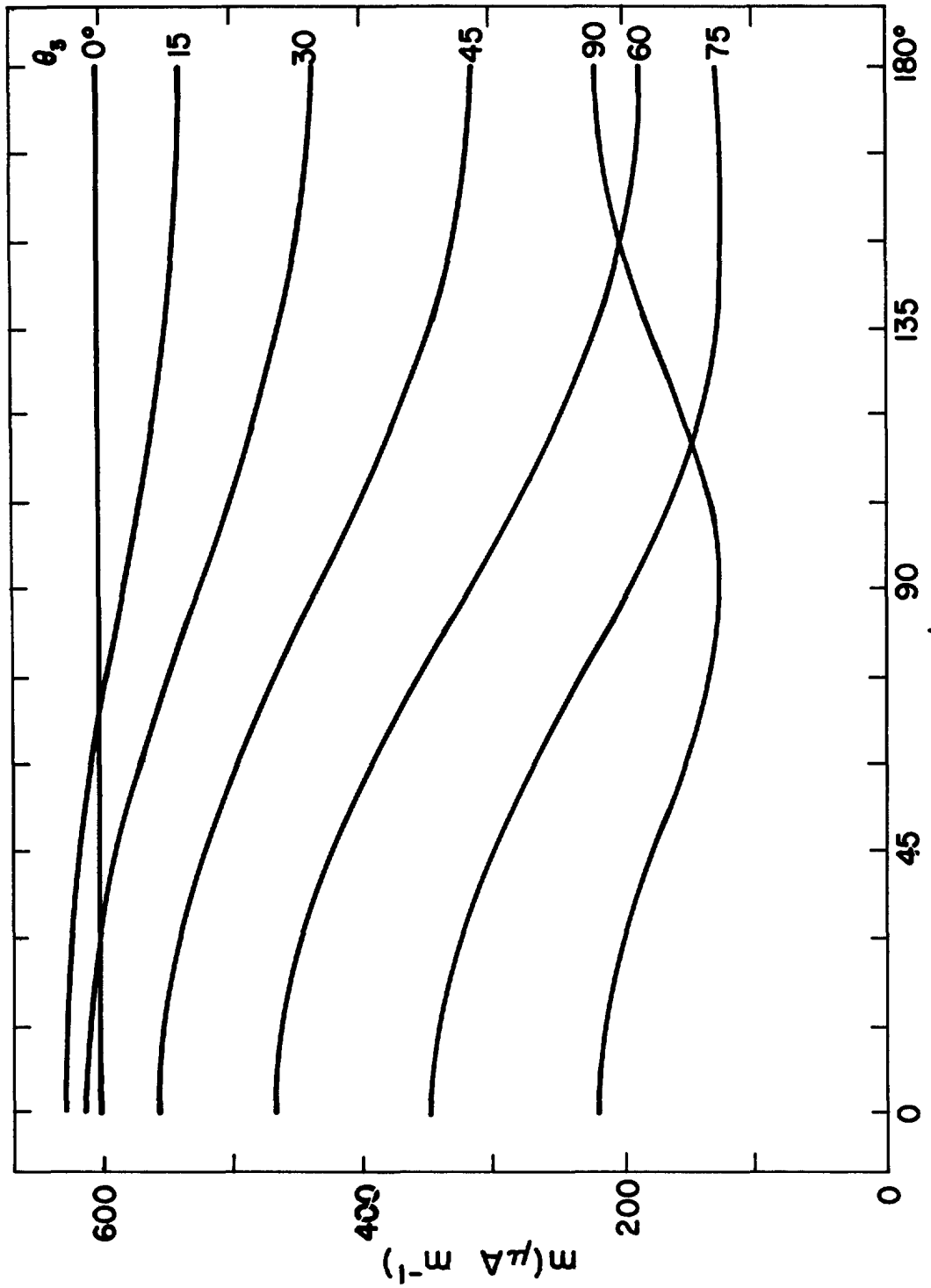

Figure 4

Induced magnetic dipole moment per unit volume in a permeable spheroid as a function of the orientation of the spheroid relative to the ambient field. Relevant parameters (Appendix A, Fig. 3) are $\mu_1/\mu_0 = 51$, $e = 4$, $\mu_0 H_0 = 60000$ nT, $\theta_0 = 17°$.

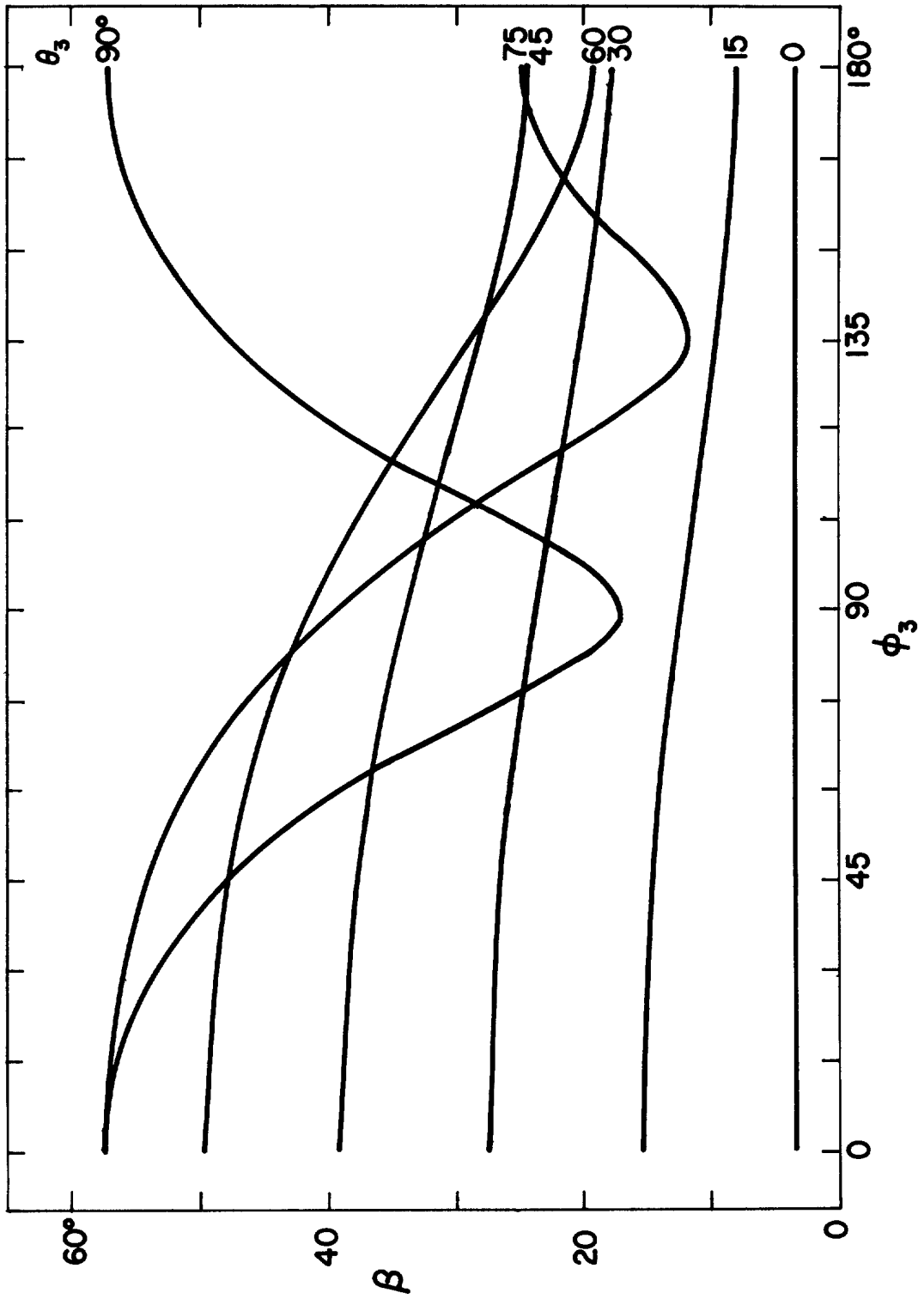

Figure 5

Polar angle of the magnetic moment of the same spheroid as in Fig. 4.

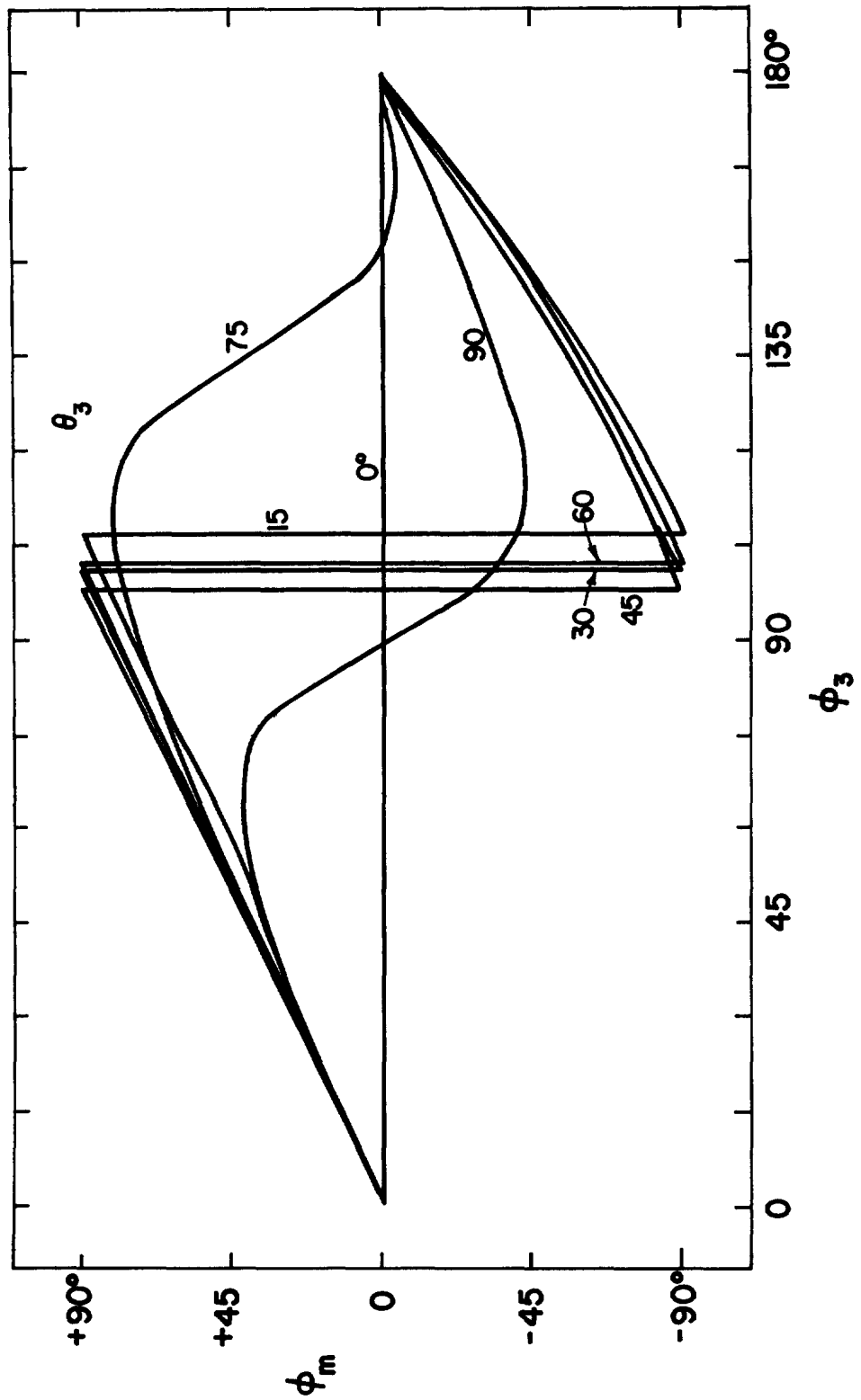

Figure 6

Azimuthal angle of the magnetic moment of the same spheroid as in Fig. 4.

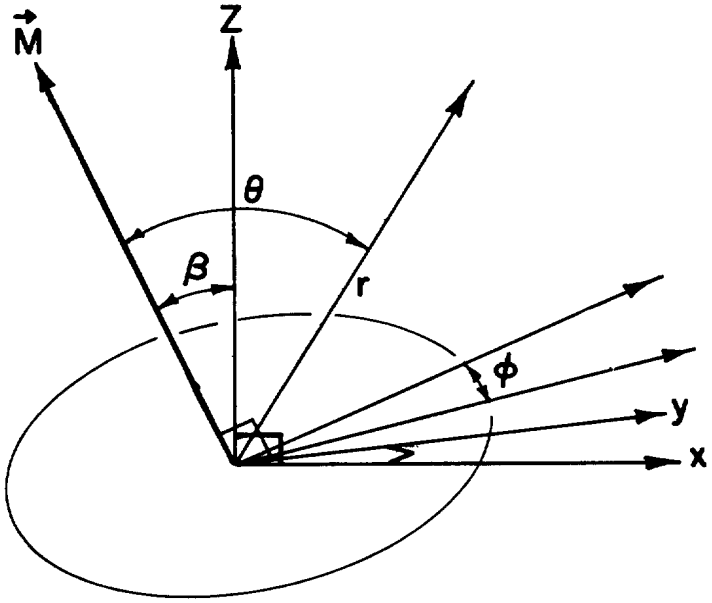

Figure 7

Relationship between cartesian and polar coordinates of a dipole.

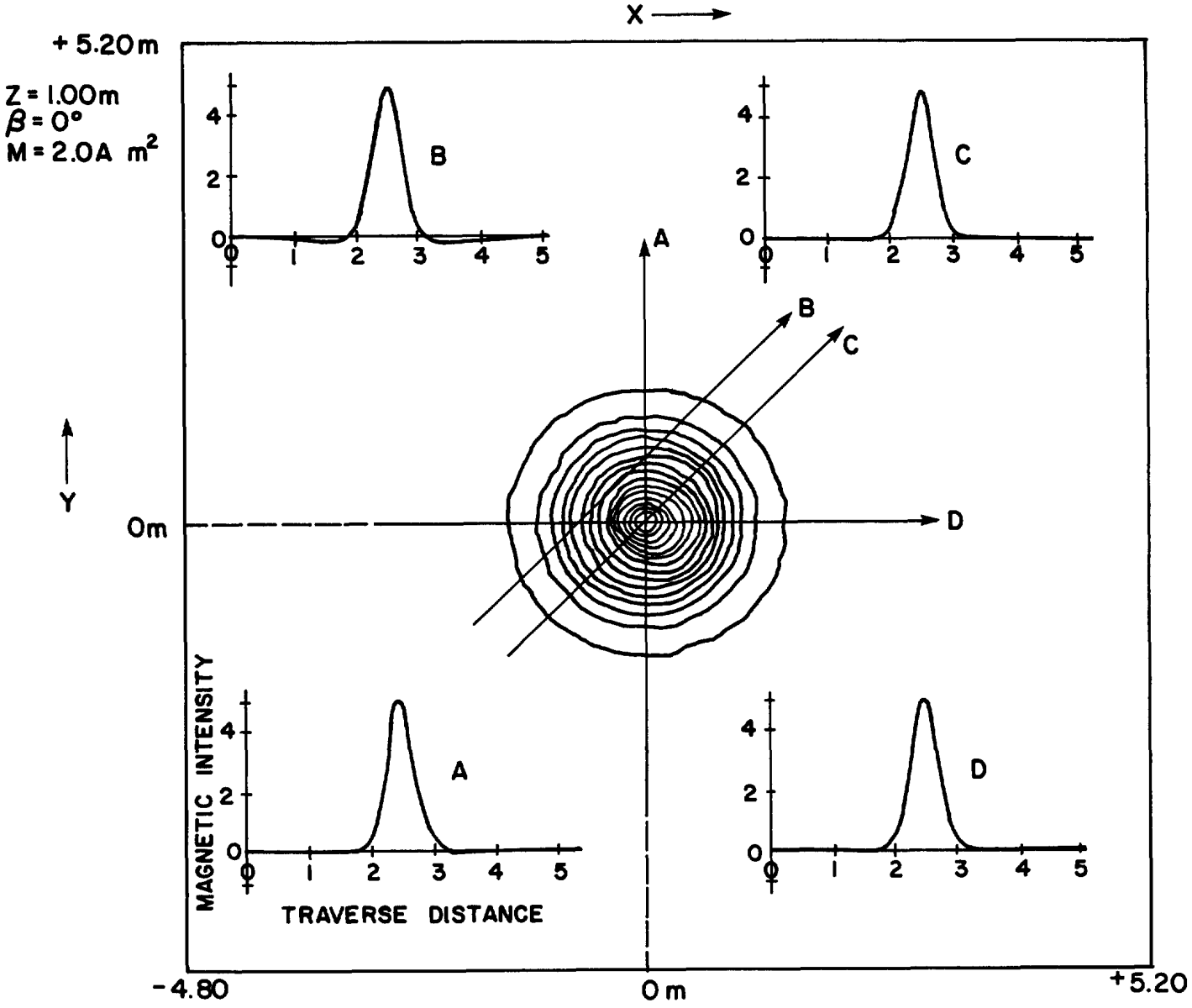

Figure 8

Lines of equal field intensity (vertical component) for a dipole with parameters (Appendix B) as indicated on the figure. Profiles corresponding to lettered paths and normalized in path length and intensity, are shown in the corners of the figure.

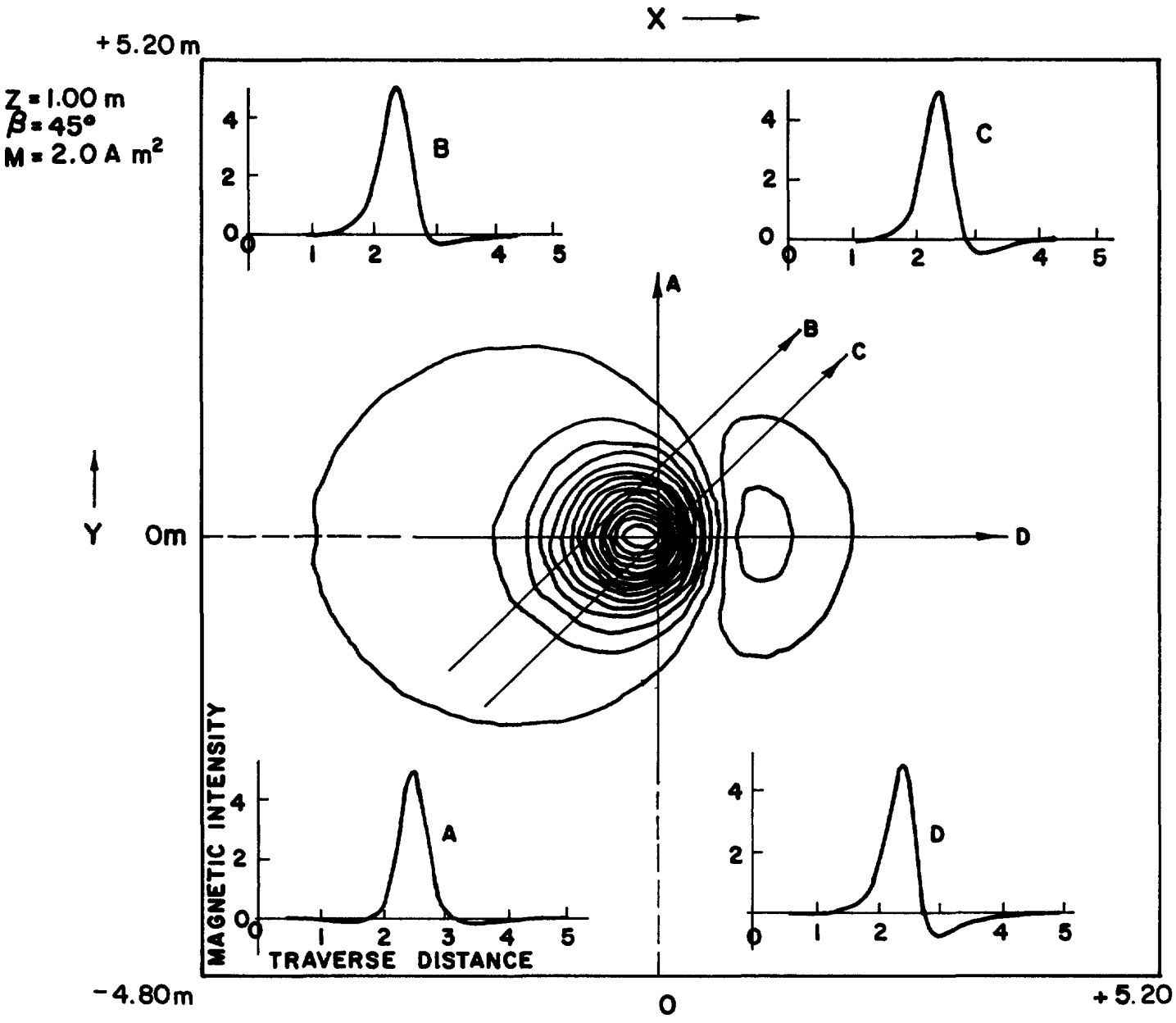

Figure 9

Lines of equal field intensity (vertical component) for a dipole with parameters the same as those of Fig. 8, except that β = 45°.

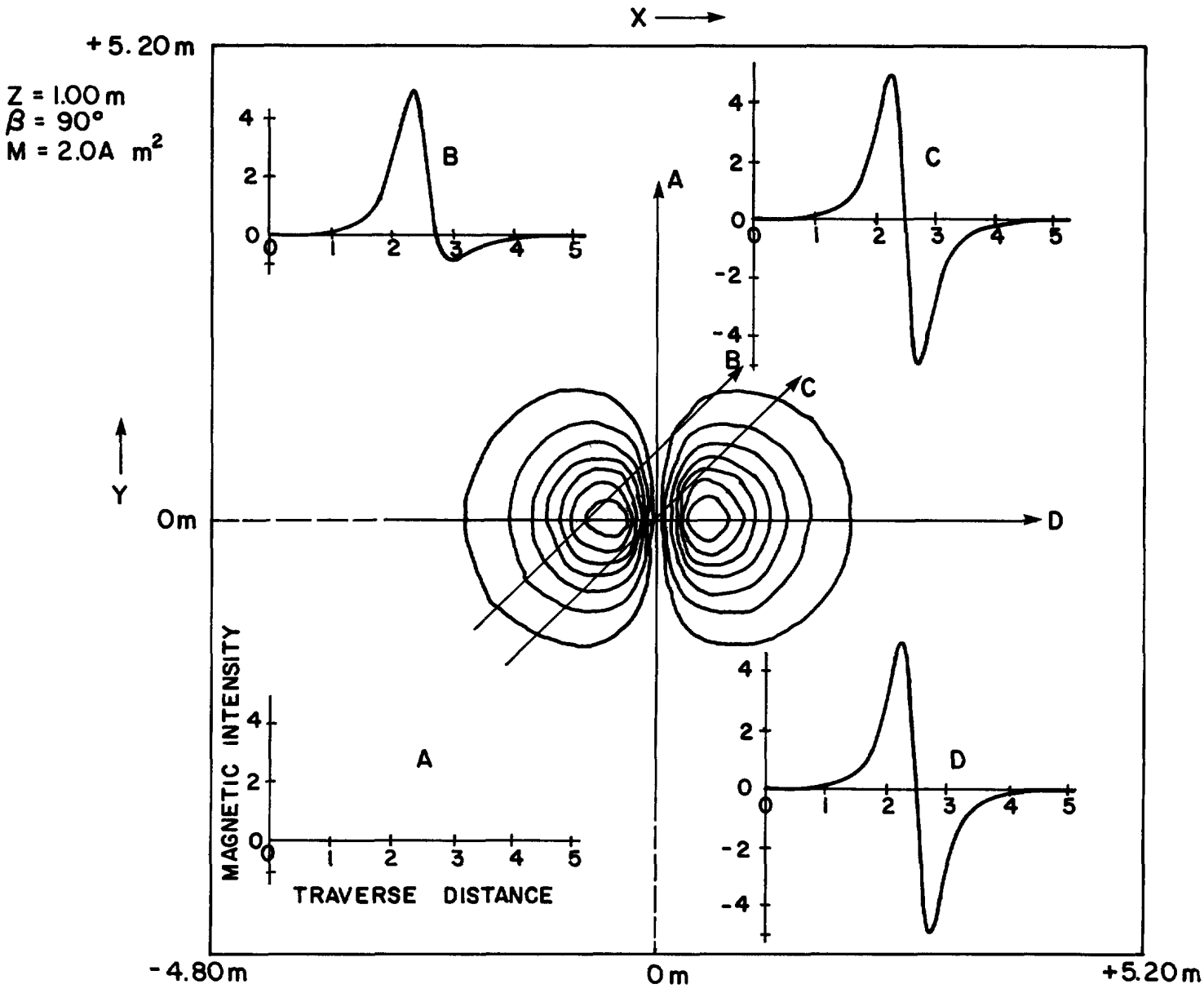

Figure 10

Lines of equal field intensity (vertical component) for a dipole with parameters the same as those of Fig. 8, except that β = 90°.

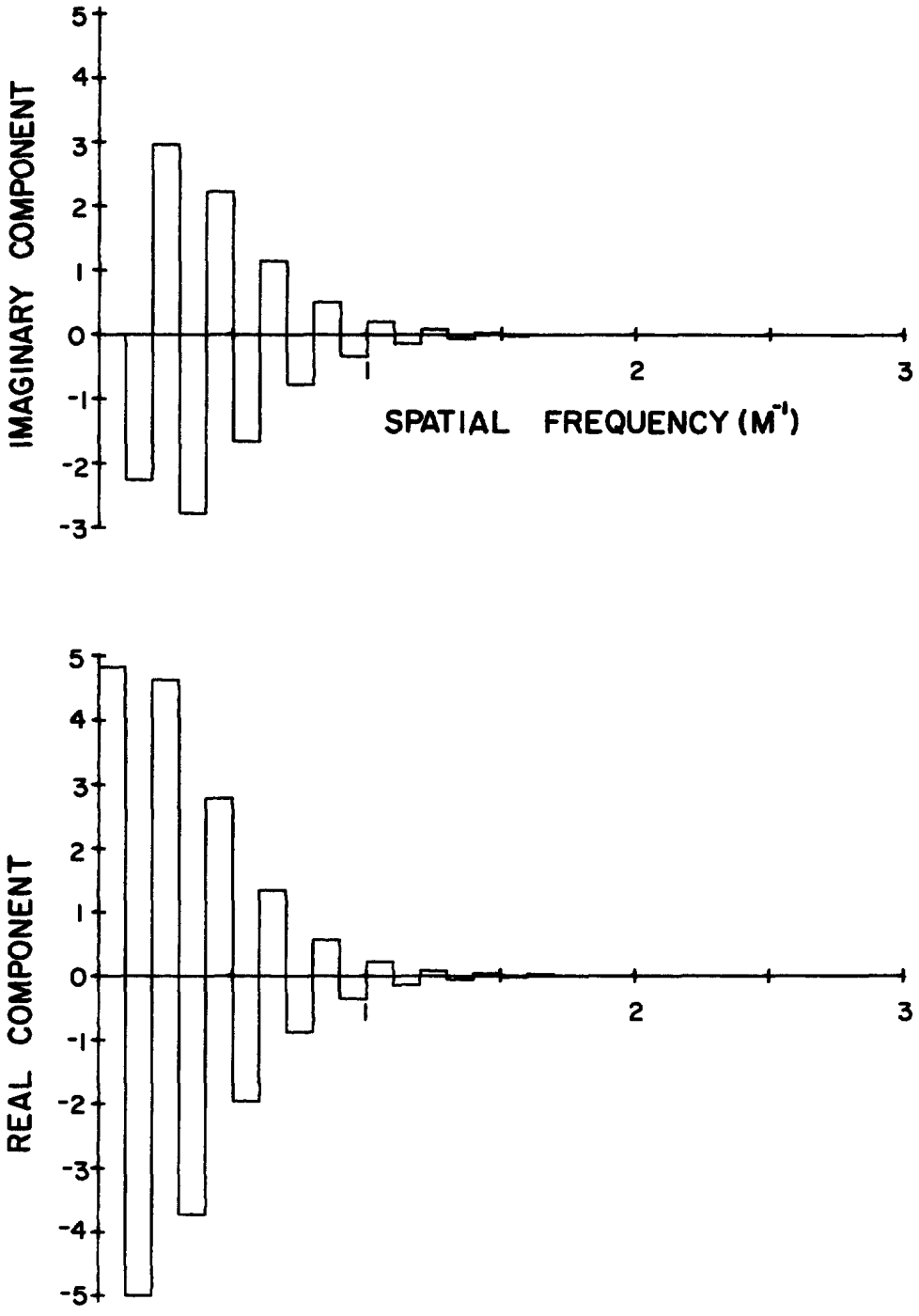

Figure 11

Fast Fourier Transform of a typical single profile of a magnetic dipole field. Dipole parameters are $z = 1.0$ m, $\beta = 45°$, $\alpha = 0°$, $x'_o = 0$ m, $y'_o = 0$ m, $M = 2.0$ Am^2. Profile was 10 m long and sampled at 0.01 m intervals to yield a possible frequency domain of 0.98 m^{-1} to 500 m^{-1}. Transform is normalized.

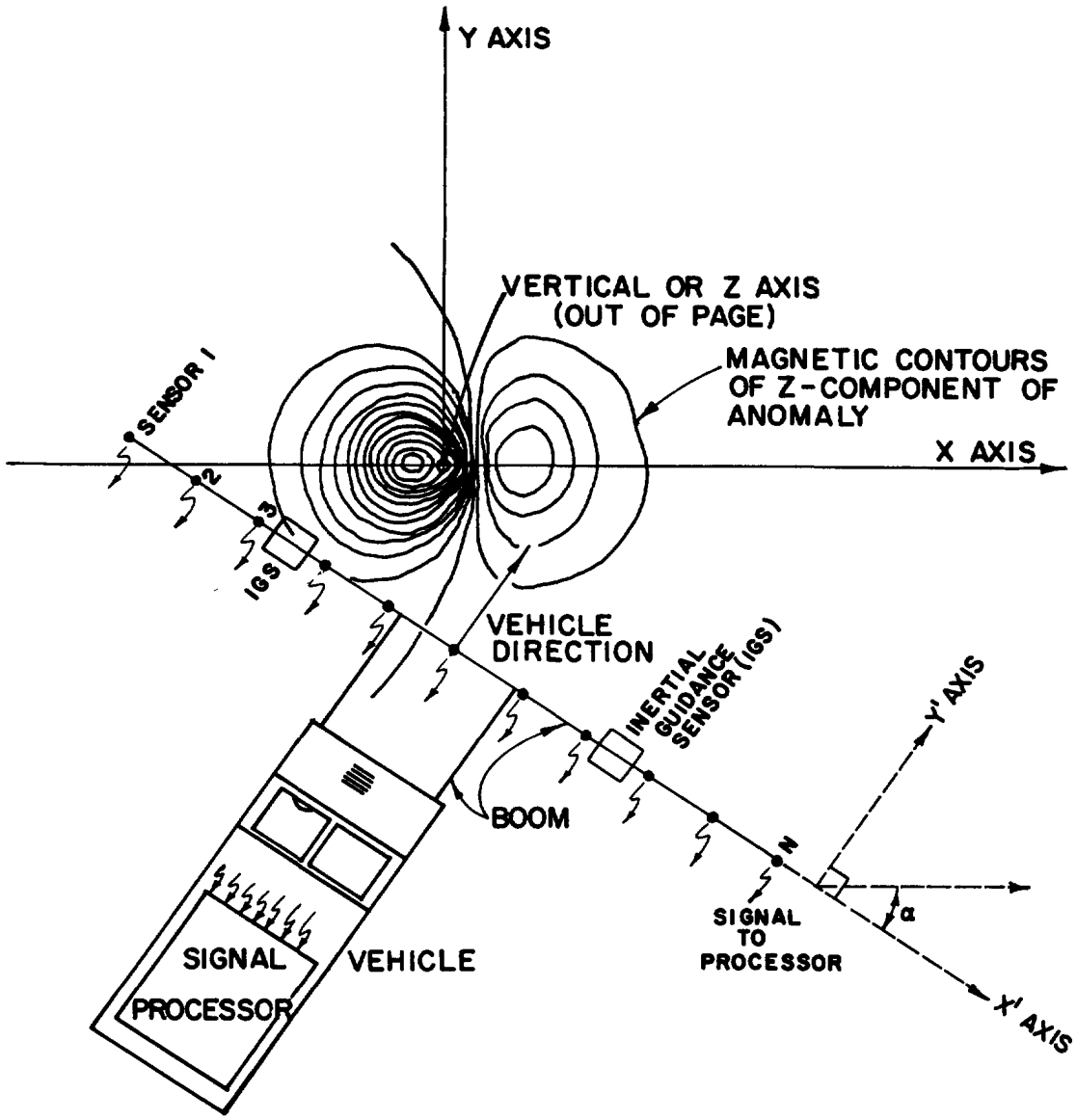

Figure 12

Geometry for horizontal linear array methods of magnetic detection (Section II).

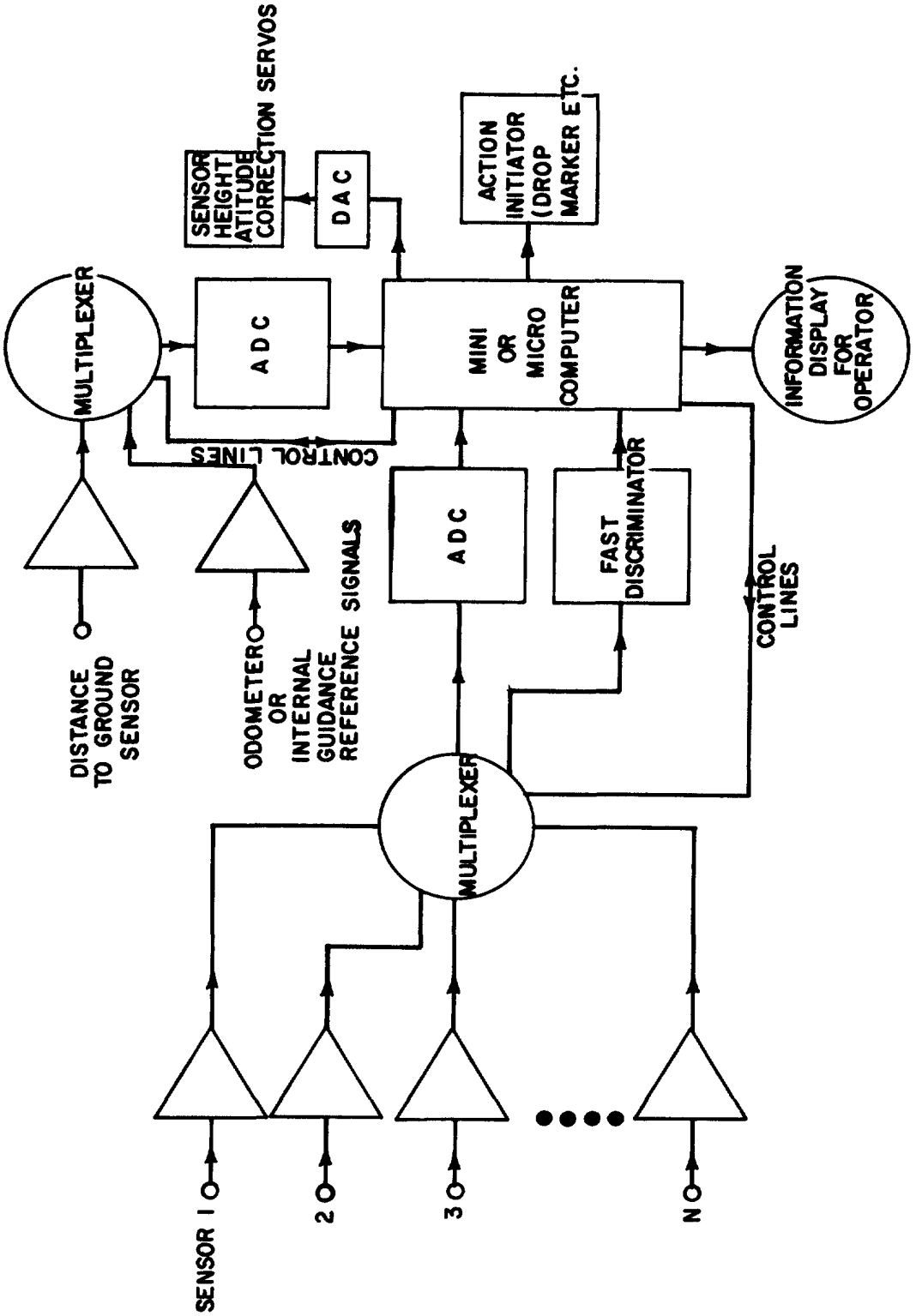

Figure 13

Possible electronic configuration for horizontal linear array methods of magnetic detection (Section II).

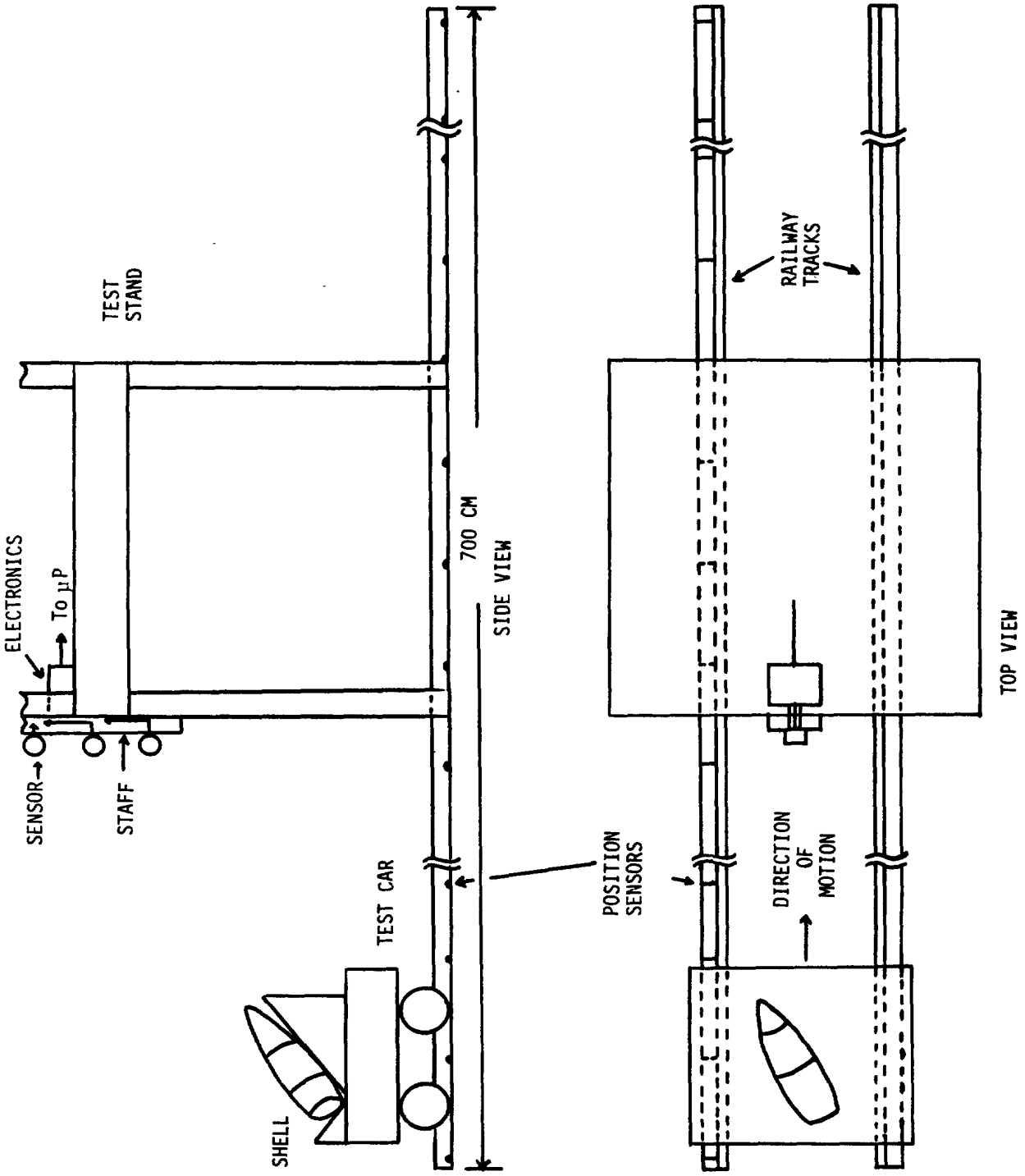

Figure 14

Experimental configuration for magnetic dipole field measurements.

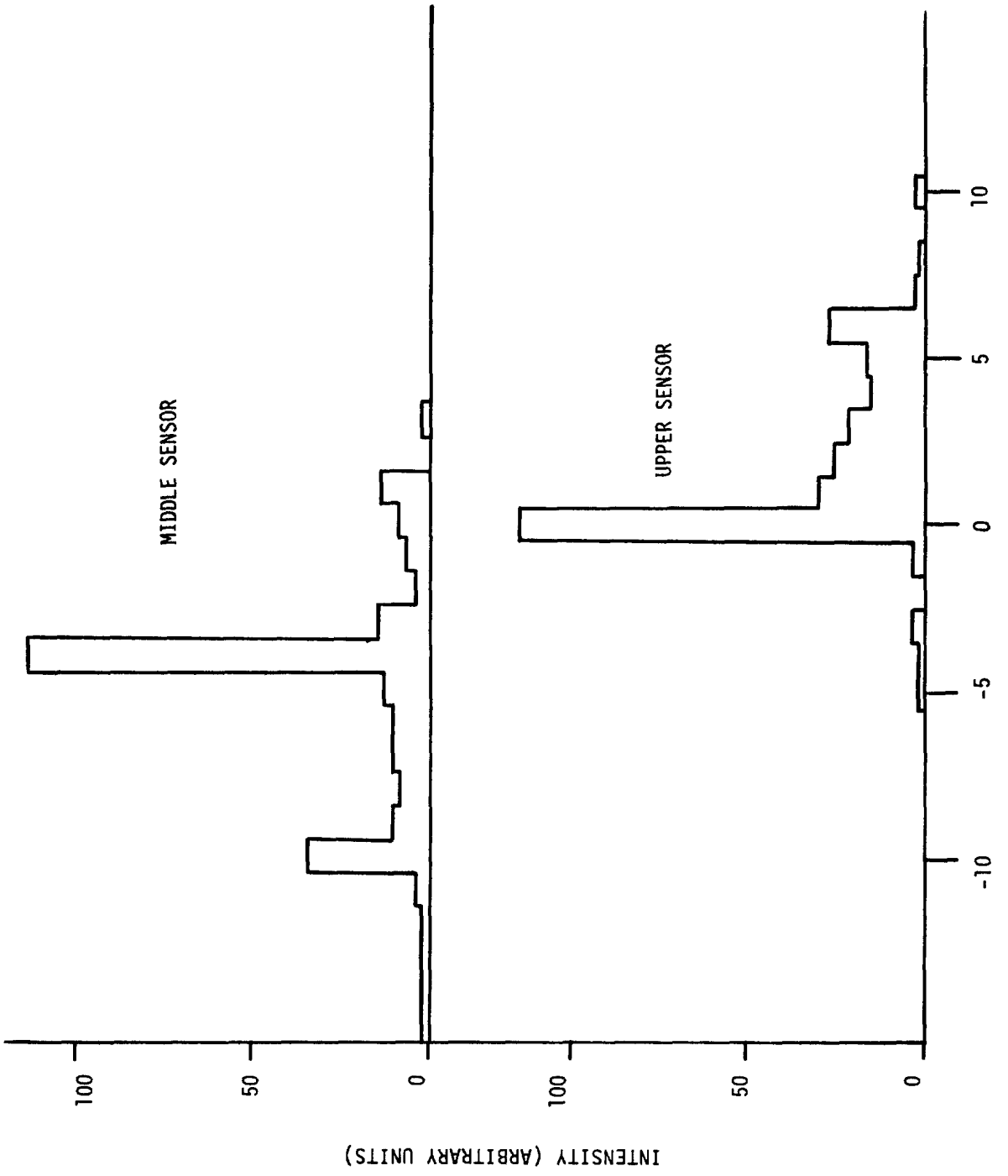

Figure 15 - Frequency histograms of noise on the electronic channels of the upper and middle sensors of Fig. 14.

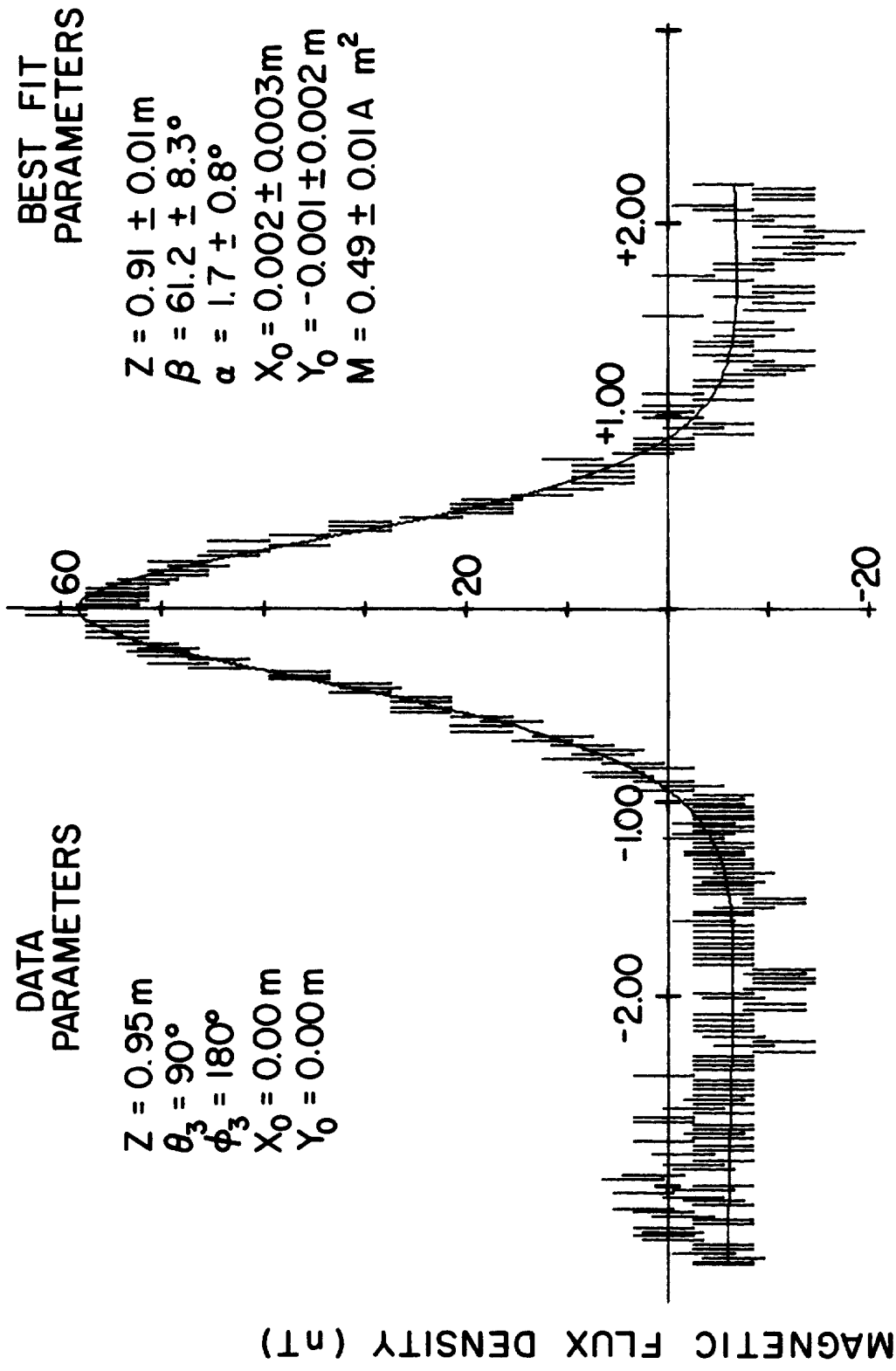

Figure 16 - Measured magnetic flux density (vertical component) profile of a 14 kg 105 mm shell from the experiment of Section II. Uncertainty in data values is denoted by length of vertical bars. Solid curves are derived from best fit parameters.

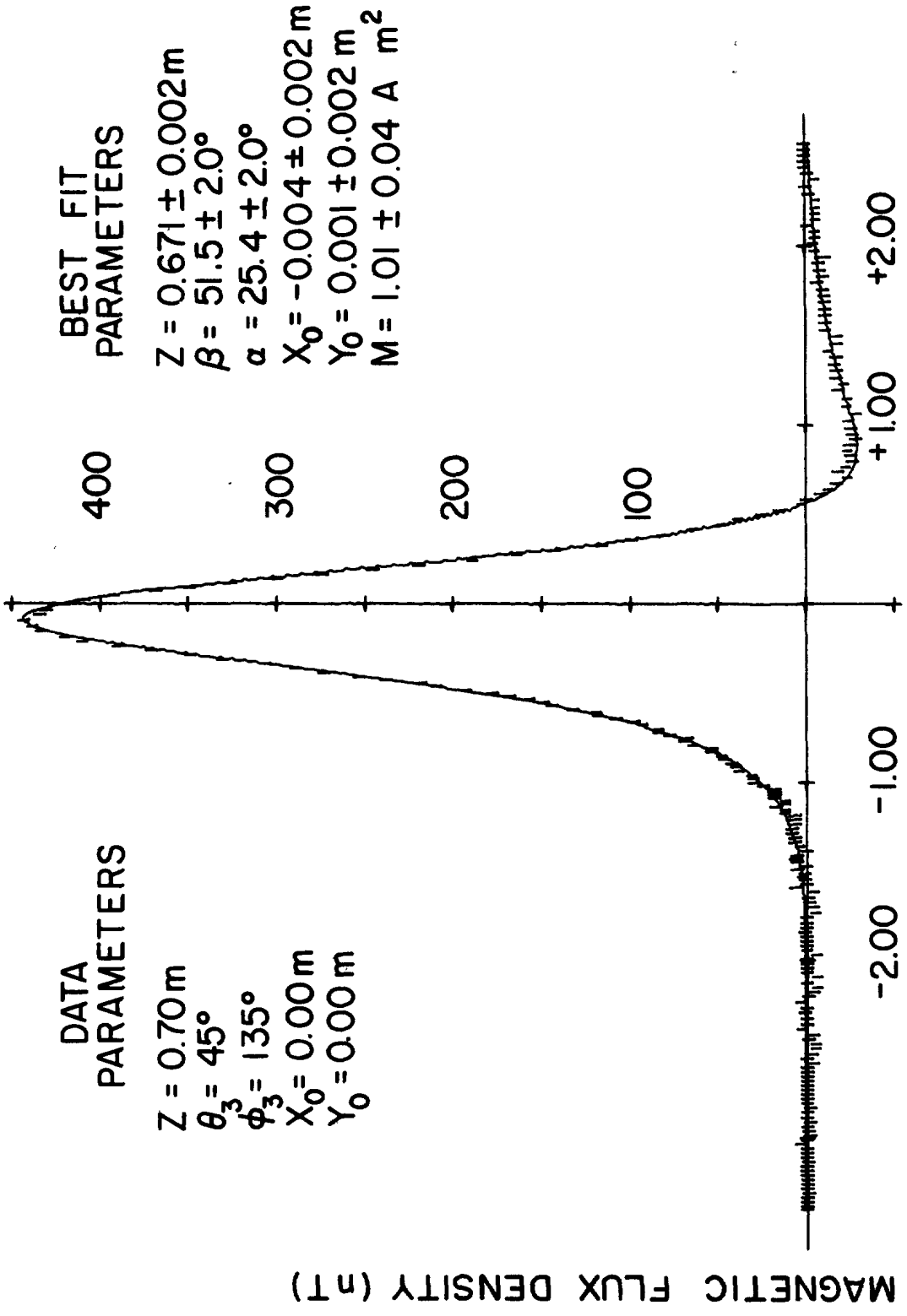

Figure 18 - Measured magnetic flux density (vertical component) profile of a 14 kg 105 mm shell from the experiment of Section II.

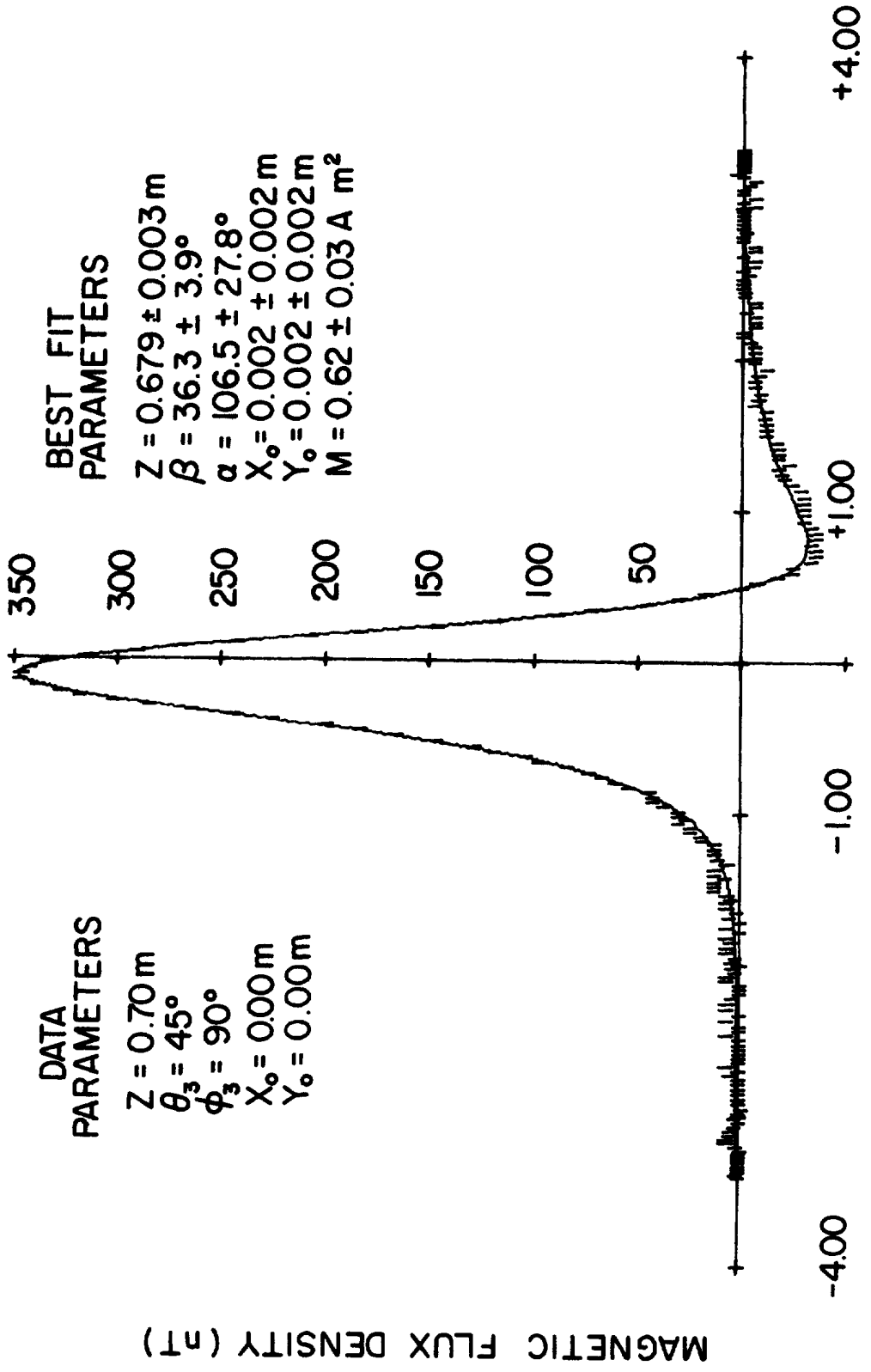

Figure 19 - Measured magnetic flux density (vertical component) profile of a piece of 105 mm shrapnel (essentially intact but hollowed out) from the experiment of Section II.

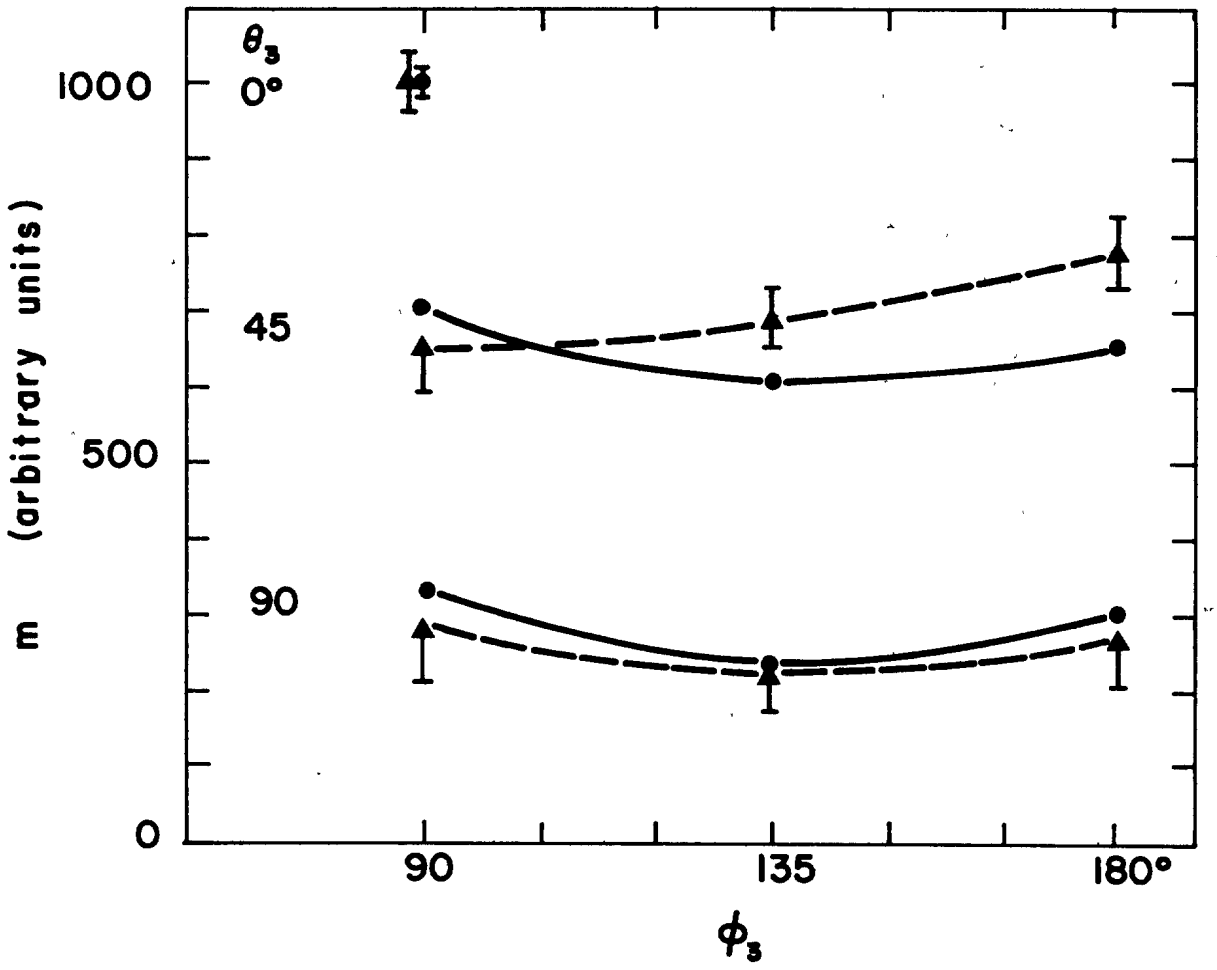

Figure 20

Measured dipole moments per unit volume as a function of orientation relative to the ambient field. Orientation parameters, θ_3 and ϕ_3 are defined as for a spheroid (Appendix A) with the symmetry axis of the shell being the 3-axis. The dots correspond to a 105 mm howitzer shell and the triangles to a piece of 105 mm shrapnel (hollowed out but intact). Uncertainties, where not shown by error bars, are smaller than the dots or triangles. Values are individually normalized to the maximum value for each object type. The curves are merely to show trends.

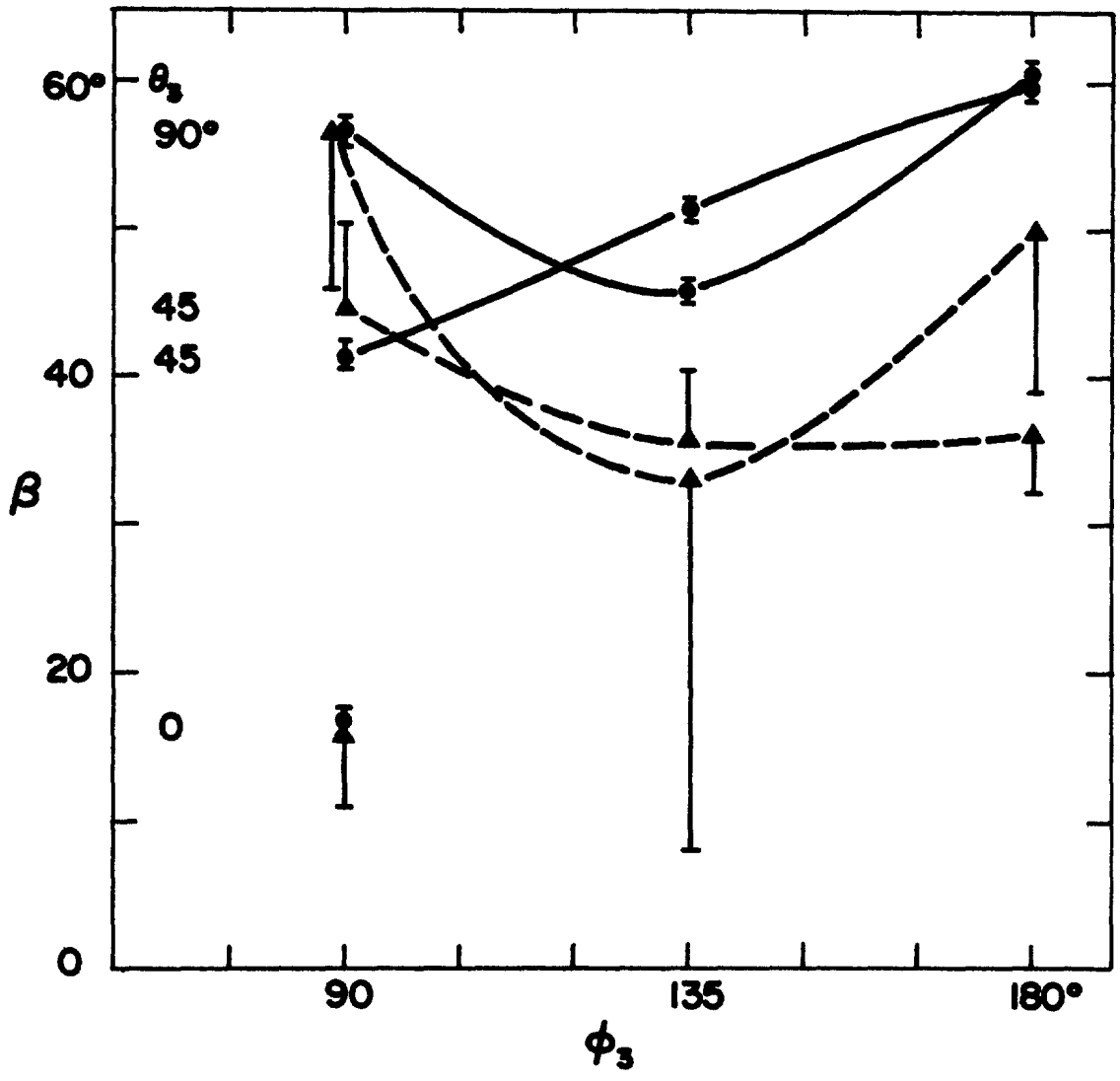

Figure 21

Polar angle of the dipole moments of Fig. 20.

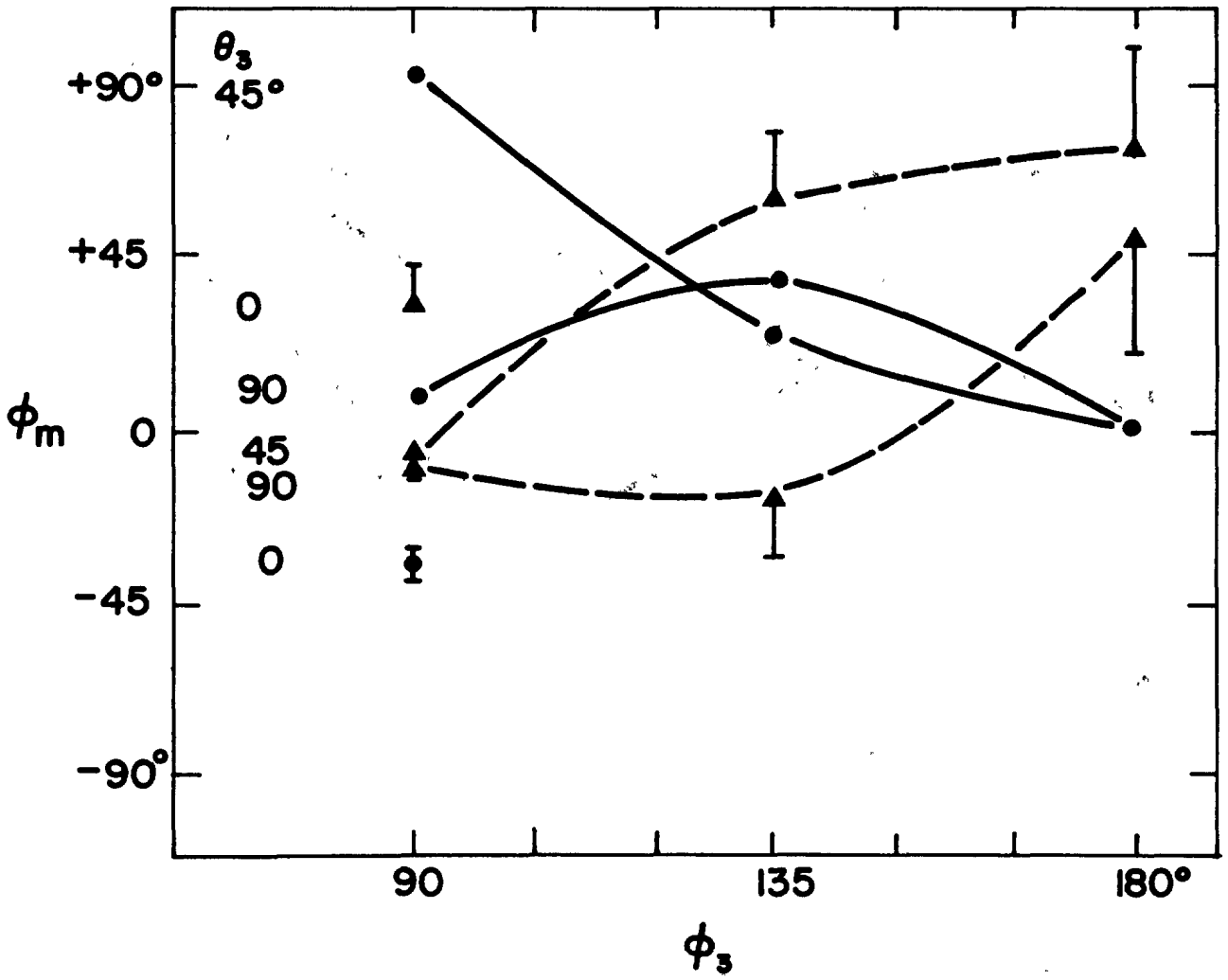

Figure 22

Azimuthal angle of the dipole moments of Fig. 20.

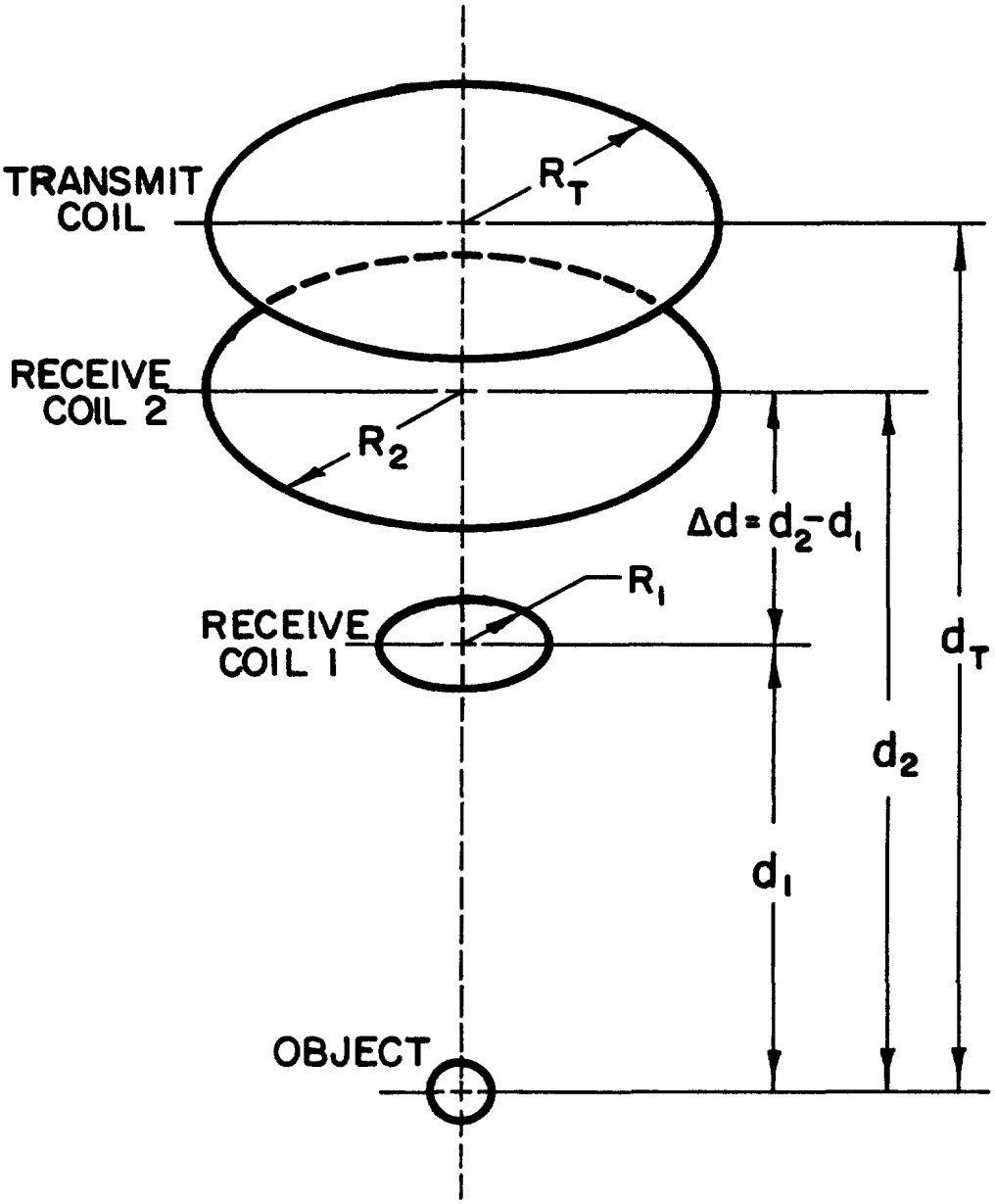

Figure 23

Geometrical arrangement of coils.

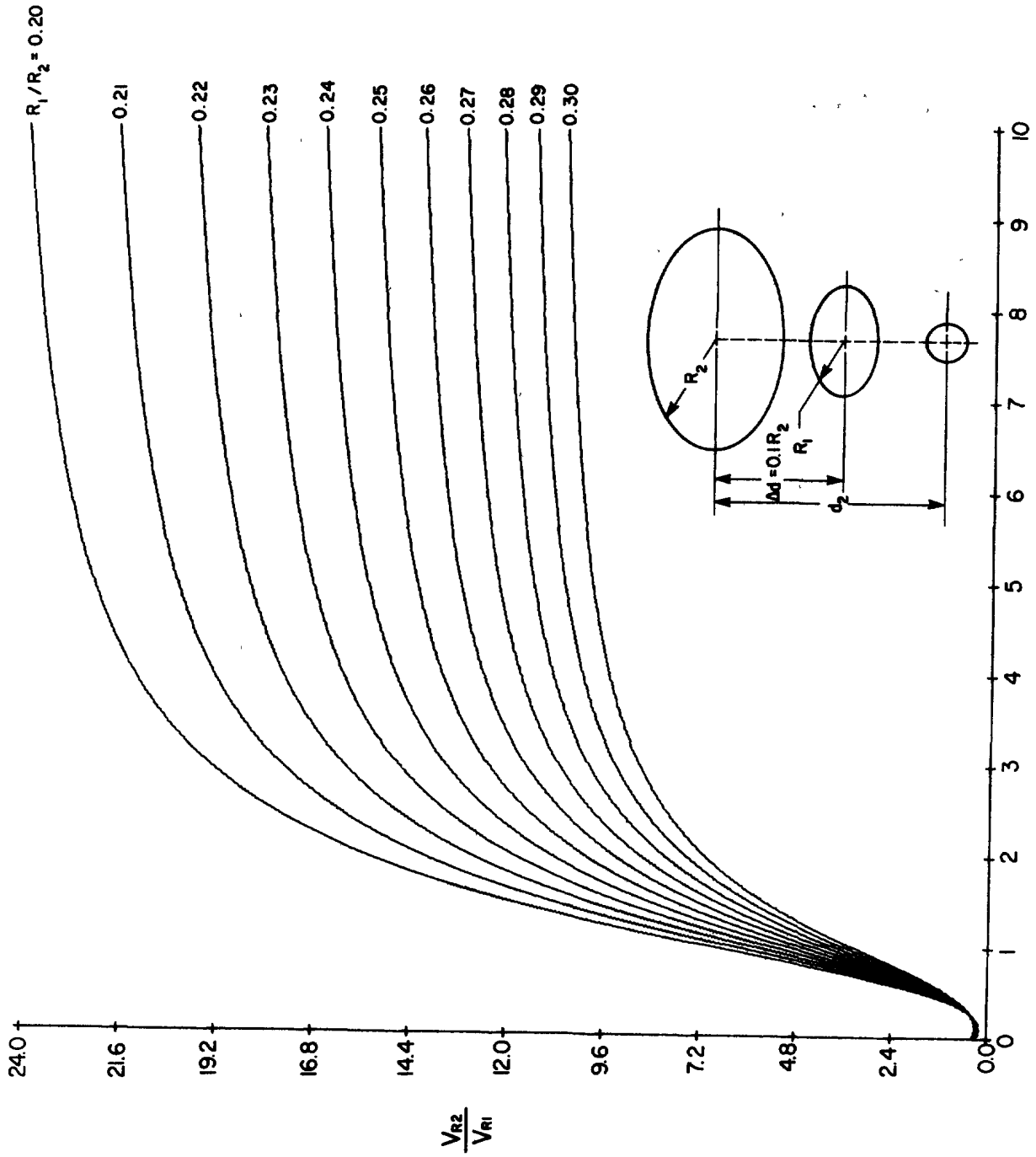

Figure 24 Calibration curves for the determination of depth.

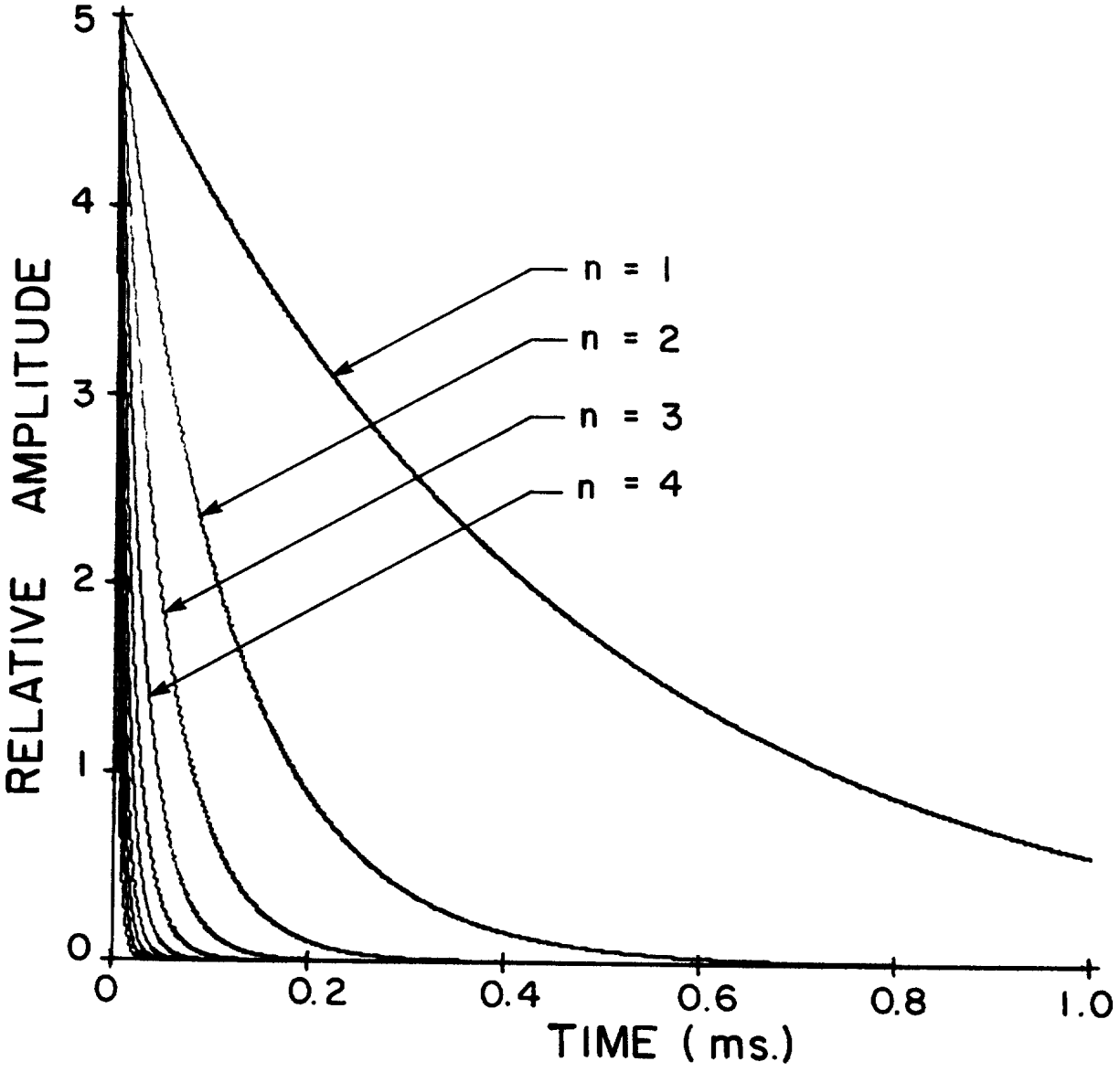

Figure 25

Behaviour of the first ten terms of the response of a non-permeable sphere.

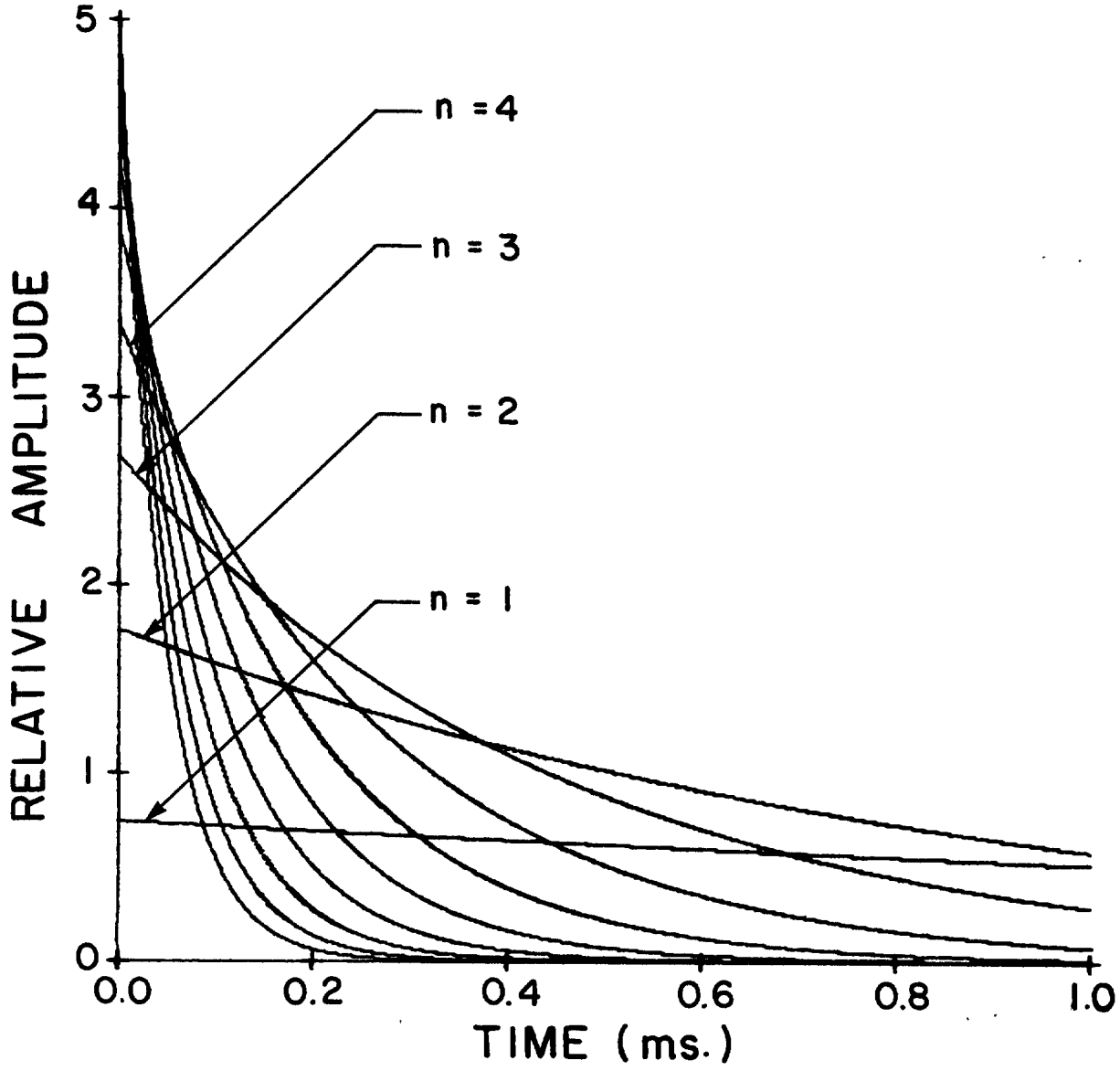

Figure 26

Behaviour of the first ten terms of the response of a permeable sphere.

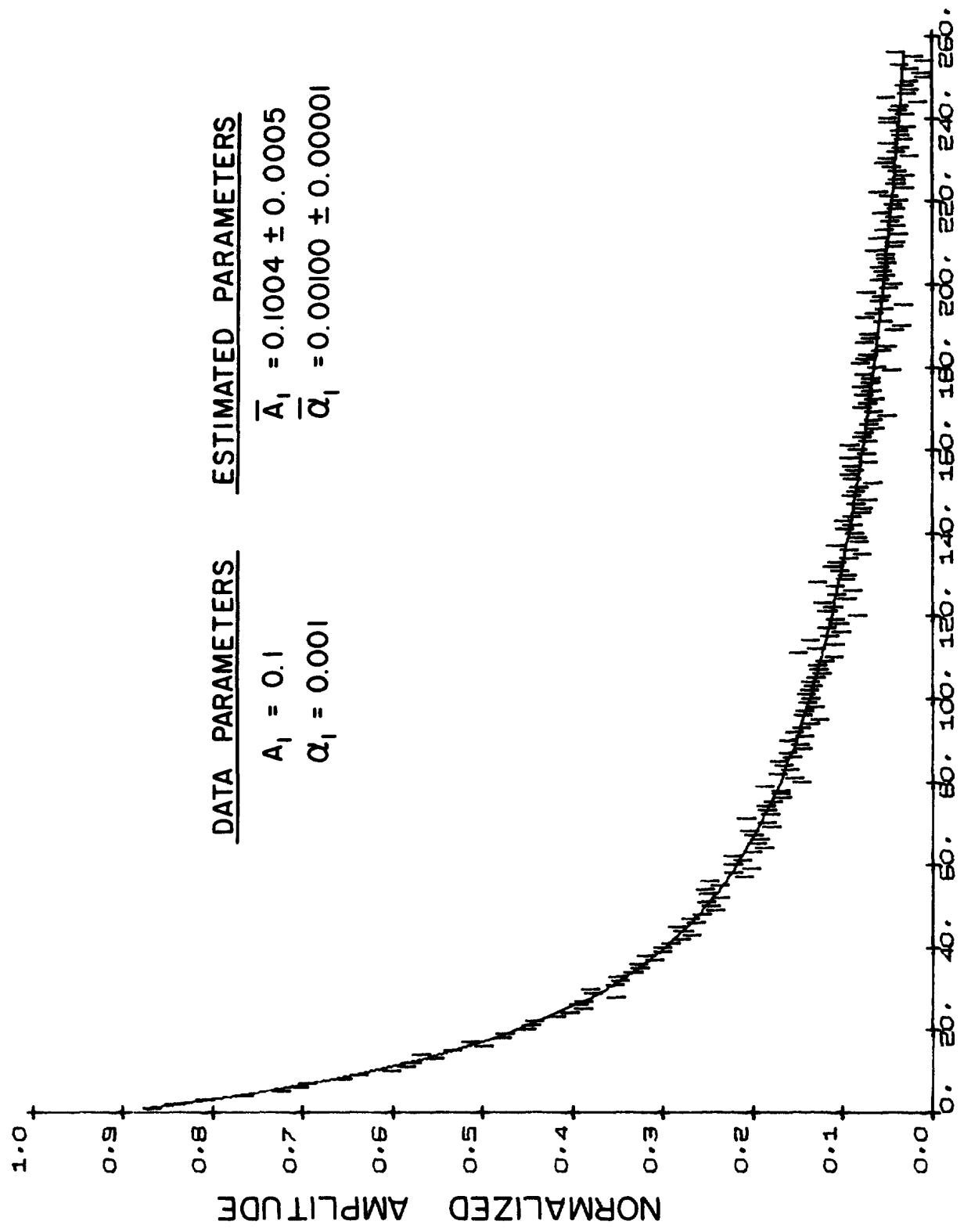

Figure 27 - Sum of ten exponentials fitted to data simulated by the sum of ten exponentials with added Gaussian noise of standard deviation 0.01.

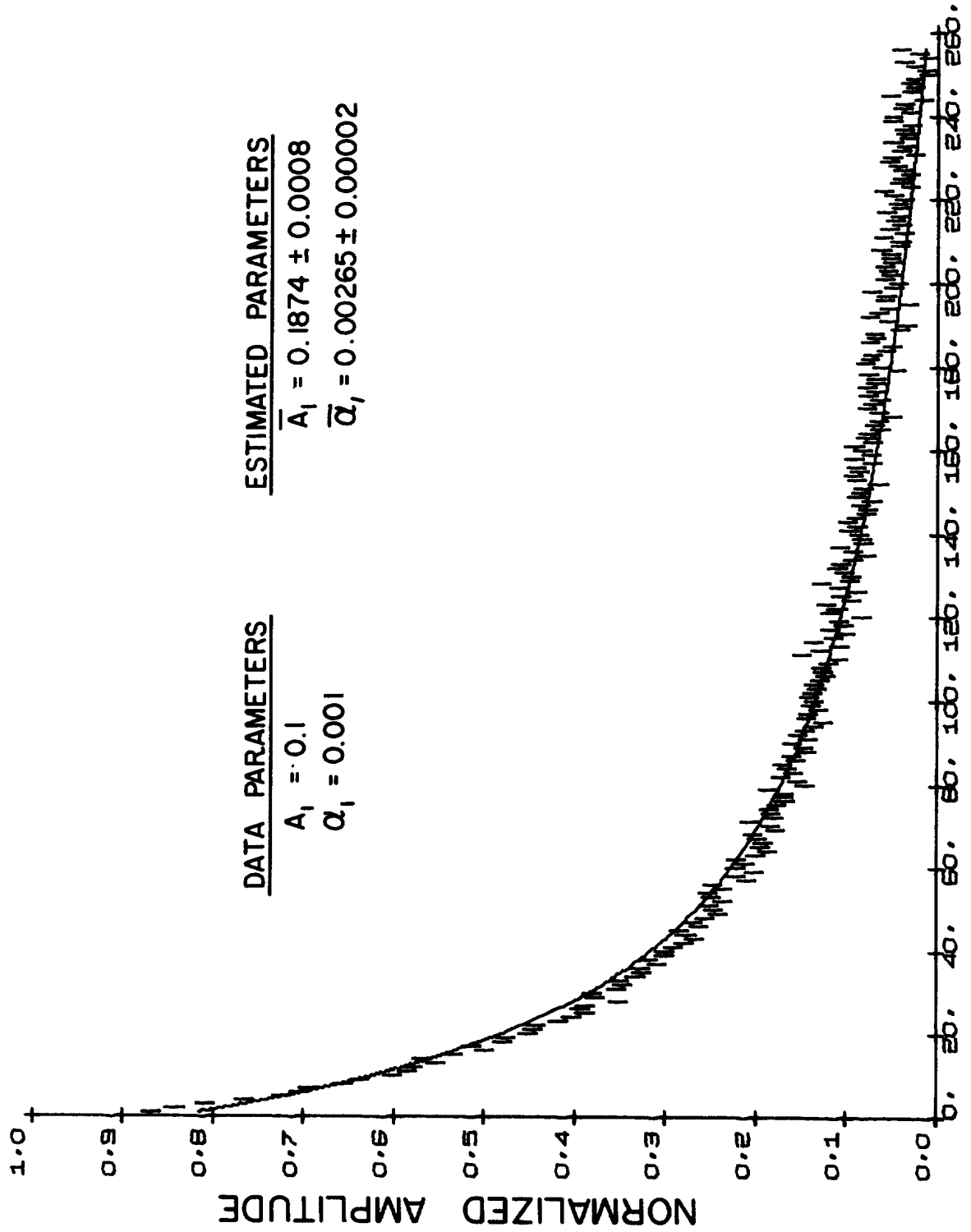

Figure 28 - Sum of five exponentials fitted to the same data as in Fig. 27.

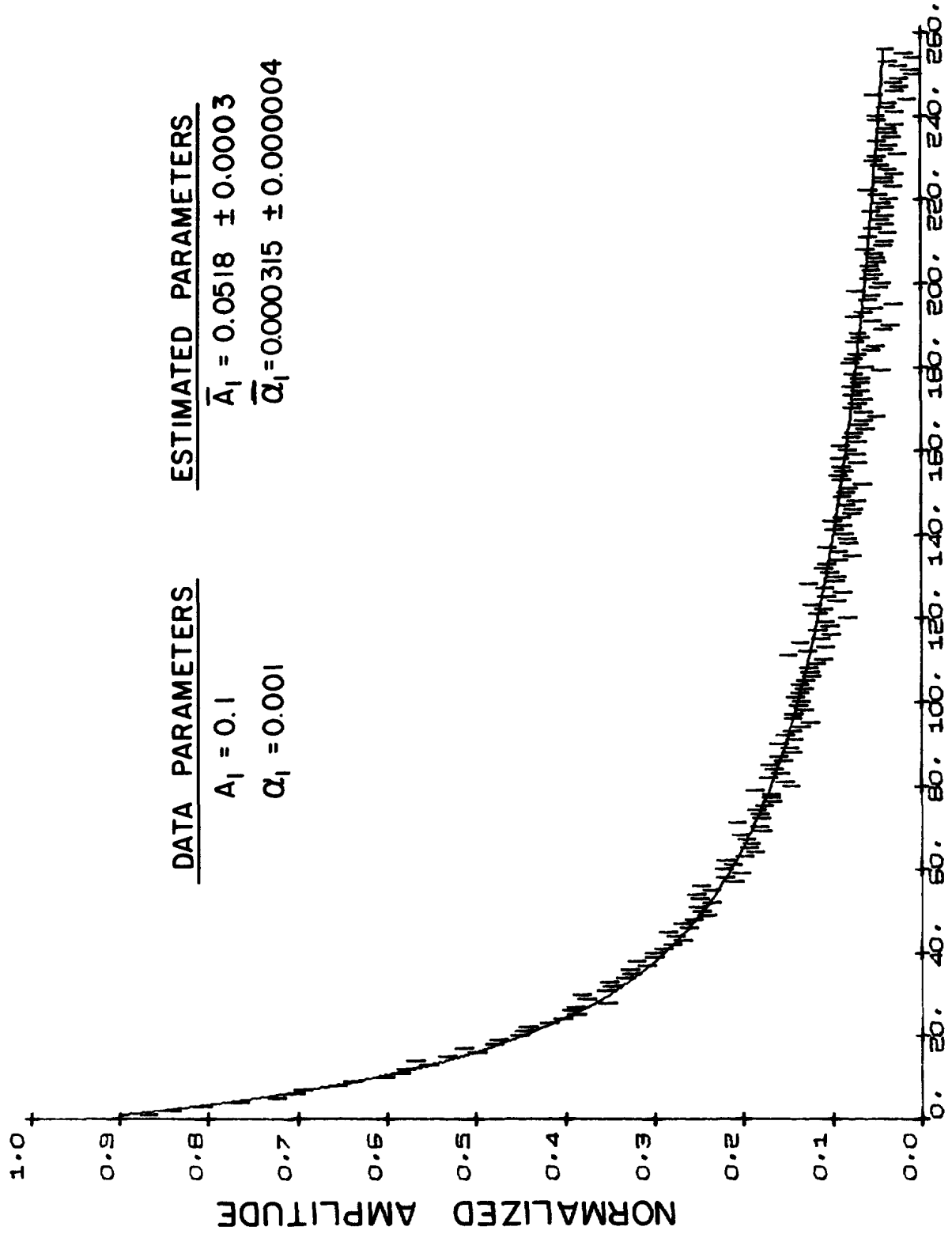

Figure 29 - Sum of twenty exponentials fitted to the same data as in Figs. 27 and 28.

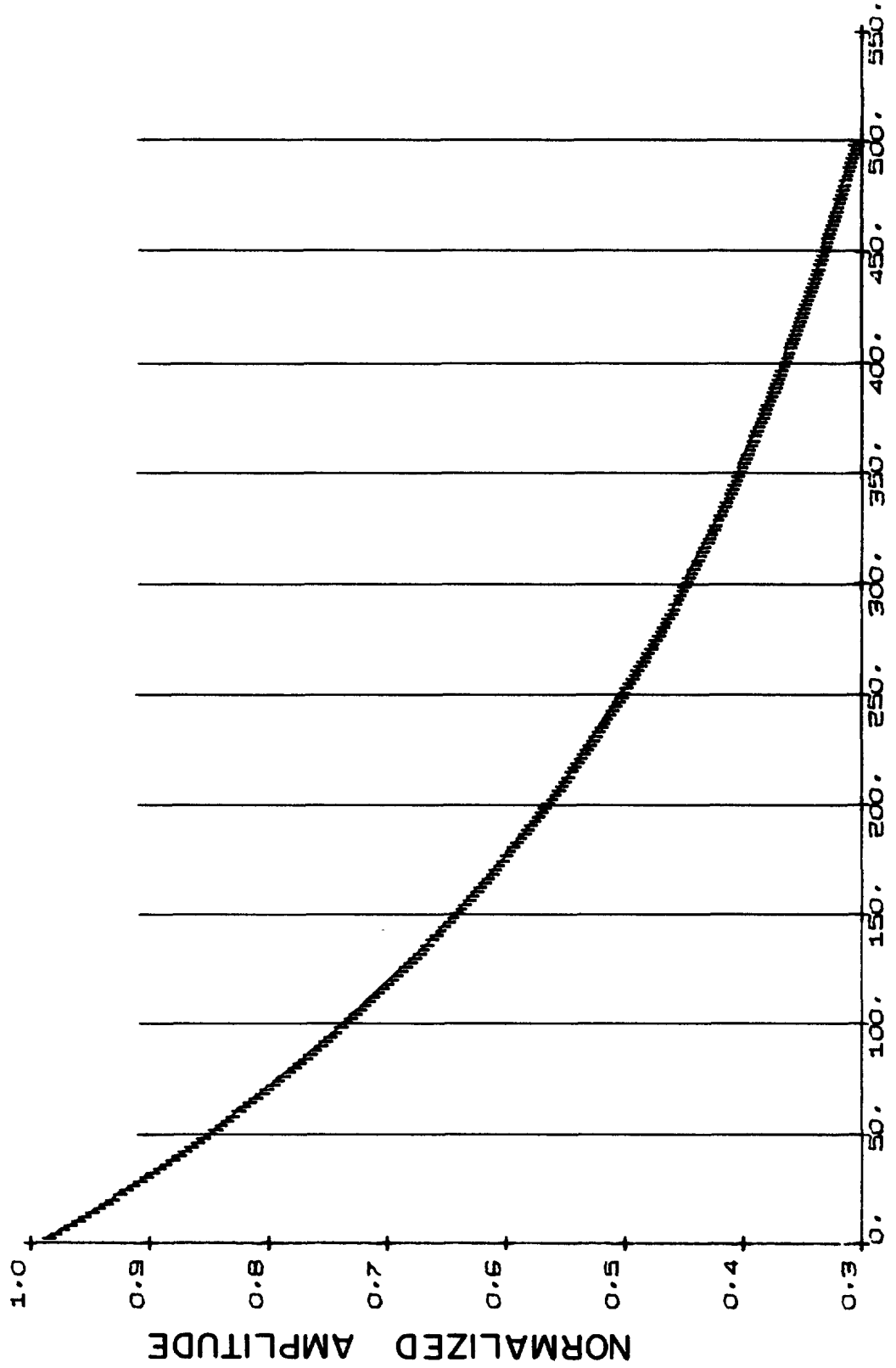

Figure 30 - Single exponentials fitted to segments of simulated data. Parameters of the object are a = 0.0481 m, μ_r = 21, $\sigma = 10^7$ S/m. Noise standard deviation is 0.005.

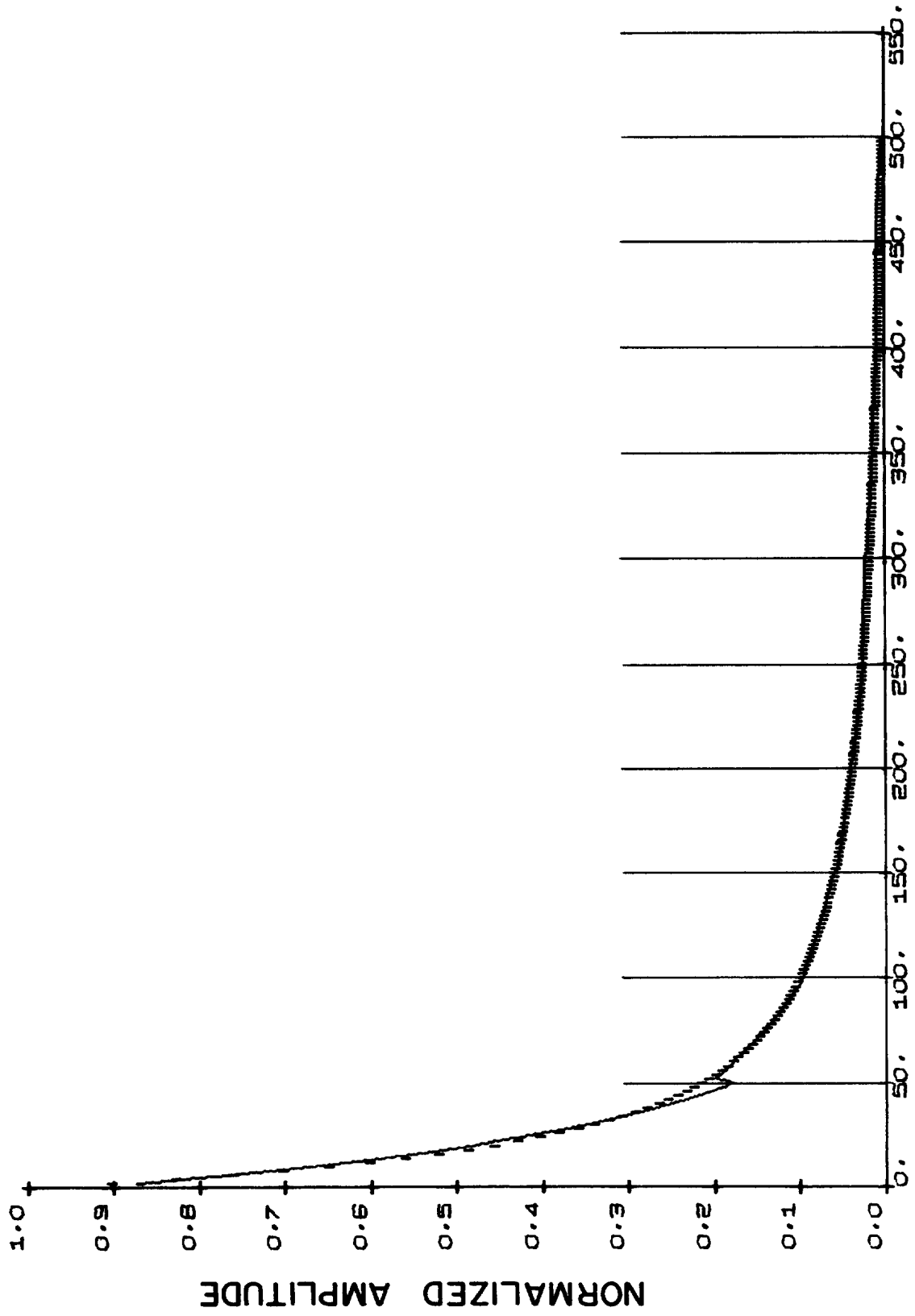

Figure 31 - Single exponentials fitted to segments of simulated data. Parameters of the object are a = 0.0127 m, μ_r = 21, $\sigma = 10^7$ S/m. Noise standard deviation is 0.005.

UNCLASSIFIED

This Sheet Security Classification

DOCUMENT CONTROL DATA - R & D

(Security classification of title, body of abstract and indexing annotation must be entered when the overall document is classified)

1 ORIGINATING ACTIVITY

DEFENCE RESEARCH ESTABLISHMENT SUFFIELD

2a. DOCUMENT SECURITY CLASSIFICATION

UNCLASSIFIED

2b. GROUP

3 DOCUMENT TITLE

DETECTION AND IDENTIFICATION OF BURIED ORDNANCE BY MAGNETIC AND ELECTROMAGNETIC MEANS (U)

4 DESCRIPTIVE NOTES (Type of report and inclusive dates)

SUFFIELD REPORT

5 AUTHOR(S) (Last name, first name, middle initial)

Das, Y., McFee, J.E., and Bell, M.

6 DOCUMENT DATE	7a. TOTAL NO. OF PAGES	7b. NO. OF REFS
June 1981	111	23

8a. PROJECT OR GRANT NO.	9a. ORIGINATOR'S DOCUMENT NUMBER(S)
27B10	SUFFIELD REPORT No. 283
8b CONTRACT NO.	9b. OTHER DOCUMENT NO.(S) (Any other numbers that may be assigned this document)

10. DISTRIBUTION STATEMENT

QUALIFIED REQUESTERS MAY OBTAIN COPIES OF THIS DOCUMENT FROM THEIR DEFENCE DOCUMENTATION CENTER

11. SUPPLEMENTARY NOTES	12. SPONSORING ACTIVITY

13. ABSTRACT

There is presently a need for clearing old army ranges of buried unexploded munitions (UXM). The present operation which relies on conventional metal detectors is very slow and expensive - mainly due to the inability of these detectors to provide any information as to the depth, size or nature (shrapnel or UXM) of detected objects. This paper discusses the research effort of the Mines and Range Clearance Group at DRES, towards conceiving and implementing intelligent detectors, which could provide ordnance depth, size and possibly identity. In particular, the analysis of magnetic anomaly and pulse eddy current signatures of typical ordnance are discussed. Signal processing problems specific to these applications are indicated and the viability of various feature selection, extraction and recognition schemes are discussed.

(U)

DSIS
79-070

UNCLASSIFIED UNLIMITED

This Sheet Security Classification

KEY WORDS

Ordnance Detectors

Magnetometers

Electromagnetic Induction Detection

Remote Sensing

Eddy Current Detection

82-00209
34912

INSTRUCTIONS

1 ORIGINATING ACTIVITY Enter the name and address of the organization issuing the document

2a DOCUMENT SECURITY CLASSIFICATION Enter the overall security classification of the document including special warning terms whenever applicable

2b GROUP Enter security reclassification group number. The three groups are defined in Appendix 'M' of the DRB Security Regulations

3 DOCUMENT TITLE Enter the complete document title in all capital letters Titles in all cases should be unclassified If a sufficiently descriptive title cannot be selected without classification show title classification with the usual one-capital-letter abbreviation in parentheses immediately following the title

4 DESCRIPTIVE NOTES Enter the category of document, e g technical report technical note or technical letter If appropriate enter the type of document, e g interim, progress, summary, annual or final Give the inclusive dates when a specific reporting period is covered.

5 AUTHOR(S) Enter the name(s) of author(s) as shown on or in the document Enter last name, first name, middle initial. If military, show rank The name of the principal author is an absolute minimum requirement

6 DOCUMENT DATE Enter the date (month, year) of Establishment approval for publication of the document.

7a TOTAL NUMBER OF PAGES The total page count should follow normal pagination procedures, i.e , enter the number of pages containing information

7b NUMBER OF REFERENCES Enter the total number of references cited in the document

8a PROJECT OR GRANT NUMBER If appropriate, enter the applicable research and development project or grant number under which the document was written

8b CONTRACT NUMBER If appropriate, enter the applicable number under which the document was written

9a ORIGINATOR'S DOCUMENT NUMBER(S) Enter the official document number by which the document will be identified and controlled by the originating activity This number must be unique to this document

9b OTHER DOCUMENT NUMBER(S) If the document has been assigned any other document numbers (either by the originator or by the sponsor), also enter this number(s)

10 DISTRIBUTION STATEMENT Enter any limitations on further dissemination of the document, other than those imposed by security classification, using standard statements such as

(1) "Qualified requesters may obtain copies of this document from their defence documentation center."

(2) "Announcement and dissemination of this document is not authorized without prior approval from originating activity "

11. SUPPLEMENTARY NOTES Use for additional explanatory notes

12 SPONSORING ACTIVITY Enter the name of the departmental project office or laboratory sponsoring the research and development. Include address.

13 ABSTRACT Enter an abstract giving a brief and factual summary of the document, even though it may also appear elsewhere in the body of the document itself It is highly desirable that the abstract of classified documents be unclassified Each paragraph of the abstract shall end with an indication of the security classification of the information in the paragraph (unless the document itself is unclassified) represented as (TS), (S), (C), (R), or (U)

The length of the abstract should be limited to 20 single-spaced standard typewritten lines 7½ inches long.

14 KEY WORDS Key words are technically meaningful terms or short phrases that characterize a document and could be helpful in cataloging the document Key words should be selected so that no security classification is required Identifiers, such as equipment model designation, trade name, military project code name, geographic location, may be used as key words but will be followed by an indication of technical context.